PHARMACOKINETICS AND BIODISTRIBUTION OF LCP NANOPARTICLES

Yang Liu

A dissertation submitted to the faculty of the University of North Carolina at Chapel Hill in partial fulfillment of the requirements for the degree of Doctor of Philosophy in the Eshelman School of Pharmacy.

Chapel Hill
2012

Approved by:

Pilar Blancafort, PhD

Moo Cho, PhD

Leaf Huang, PhD

Rudolph Juliano, PhD

Rihe Liu, PhD

ii

ABSTRACT

YANG LIU: Pharmacokinetics and Biodistribution of LCP Nanoparticles
(Under the direction of Leaf Huang, Ph.D.)

Lipid/Calcium/Phosphate (LCP) nanoparticles (NPs) with a well-defined lipid bilayer-core structure are effective in encapsulating nucleic acid and silencing target genes in tumor cells following systemic injection. The pharmacokinetics and biodistribution of LCP NPs was investigated by using nanoparticles containing a tritium-labeled oligonucleotide and H460 human lung cancer in a xenograft mouse model. LCP NPs displayed a biphasic clearance profile. Approximately 5% and 25% of the injected dose was observed in the tumor and liver, respectively. Confocal microscopy showed that LCP NPs localized within hepatocytes while Kupffer cell uptake was avoided. Small angle neutron scattering (SANS) and fluorescent polyethylene glycol (PEG) quantification data suggested that 20% (mol ratio of outer lipids) PEG was grafted on the surface of LCP NPs with an entangled and collapsed conformation. Further, it was demonstrated that the delivery to hepatocytes was PEG concentration and surface lipid dependent. LCP NPs could be redirected to the reticuloendothelial system (RES) from hepatocytes by decreasing PEG concentration on the particle surface. LCP NPs with 1,2-dioleoyl-3-trimethylammonium-propane (DOTAP) exhibited higher accumulation in the liver than LCP NPs with Dioleoylphosphatidylcholine (DOPC). Analysis of NPs-bound proteins revealed that apolipoprotein E (apoE) might serve

as an endogenous targeting ligand for LCP-DOTAP NPs, but not LCP-DOTAP NPs. The enhanced liver accumulation with LCP-DOTAP NPs was reduced in apoE deficient mice. In all, characteristics of surface chemistry played important roles in influencing PK and biodistribution of LCP NPs. The significant hepatocytes uptake is of great interest to formulation design for oncologic and hepatic applications.

ACKNOWLEDGEMENTS

Contents

LIST OF TABLES

LIST OF FIGURES

LIST OF ABBREVIATIONS AND SYMBOLS

1D- or 2D-   one or two-dimensional

λ wavelength

a   monomer size

Å   Angstrom

apoE   apolipoprotein E

BBB   blood brain barrier

D   distance of two grafting sites

DOPA   Dioleoylphosphatydic acid

DOPC   Dioleoylphosphatidylcholine

DOPE   Dioleoyl-phosphatidylethanolamine

DOTAP   1,2-dioleoyl-3-trimethylammonium-propane

$DSPE\text{-}PEG_{2000}$ 1,2-distearoyl-sn-glycero-3-phosphoethanolamine-N-[poly(ethylene glycol)2000]

DSPE-PEG-CF   1,2-distearoyl-sn-glycero-3-phosphoethanolamine-N-[poly(ethylene glycol)2000-N'-carboxyfluorescein

EDTA   ethylenediaminetetraacetic acid

ESI   electrospray ionization

EPR   enhanced permeability and retention

HSA   human serum albumin

LCP   Lipid/Calcium/Phosphate

ICP-MS	inductively coupled plasma mass spectrometry
LDL	low-density lipoprotein
LDLR	low-density lipoprotein receptor
IgG	Immunoglobulin G
ID	injected dose
LPD	liposome-polycation-DNA
MALDI	matrix-assisted laser desorption/ionization
MMP	matrix metalloproteinases
MS	mass spectrometry
MW	molecular weight
N	degree of polymerization
NIR	near-infrared
NMR	nuclear magnetic resonance
NPs	nanoparticles
PAGE	polyacrylamide gel electrophoresis
PEG	polyethylene glycol
PK	pharmacokinetics
RES	reticuloendothelial system
R_F	radius of the random coil the polymer forms in solution
	Flory radius
SANS	small angle neutron scattering
SD	standard deviation
SDS	sodium dodecyl sulfate

SLD	scattering length density
TEM	transmission electron microscope
TGA	thermal gravity analysis
TOF	time-of-flight
$X_{m\text{-}b}$	concentration of grafted PEG-lipid for which the PEG chains first begin to overlap
XPS	X-ray photoelectron spectroscopy

CHAPTER 1

INTRODUCTION

Intravenously injected nanoparticles (NPs) as drug carriers provide a wide range of unique opportunities for site-specific delivery of therapeutic agents to many targets, for example tumors or the liver [1, 2]. The future of this expanding field is promising; over 20 NP therapeutics have been approved by the FDA for clinical use and many are in late-phase clinical trials [1, 3]. Safe and efficient delivery of cargos is a precondition for a successful nanoparticle-based therapy. Over the past decades, a wide range of nanoparticulate systems, such as liposomes and polymeric nanoparticles, have been used as carriers for the intravenous delivery and site-specific targeting of small molecules and macromolecular (e.g., proteins, nucleic acid) therapeutic agents. Various attempts to increase the therapeutic index of drugs while simultaneously minimizing side effects have been made in the field of drug delivery systems.

1.1   BARRIERS FOR DRUG DELIVERY BY NANOPARTICLES

In general, nanoparticles (NPs) refer to solid, colloidal particles that range from 10 to 1000 nm in size. To be used as drug carriers, the cargo is dissolved, entrapped, adsorbed, attached or encapsulated in the nanostructed material [4]. Nanoparticle therapeutics possess

desirable features for medical applications including (i) protection of cargo drugs from enzymatic or hydrolytic degradation, (ii) increased solubility and drug loading capacity, (iii) sustained and controlled release of drugs, and (iv) preferential accumulation at the site of interest through the enhanced permeability and retention (EPR) effect [5]. Despite these advantages, injected NPs must overcome both kinetic and physical barriers after administration. This is especially true for biopharmaceutical products — that is, peptides, proteins and nuclei acids. After the nanoparticle formulation is injected into a periphery vein it must protect the cargo molecules from enzymatic degradation by endogenous nucleases. The formulation should also avoid aggregation with both blood and extracellular elements and the subsequent uptake by phagocytes (**Figure. 1.1a**). This can be accomplished by PEGylation which will be discussed in more detail below. The nanoparticles navigate in the bloodstream and then travel to the lung, which contains the first capillary bed as an initial mechanical filtration barrier [6]. Large or highly positively charged nanoparticles are trapped in the lung [7, 8]. If the nanoparticles are small enough and neutrally or negatively charged, they will leave the lung and enter into the systemic circulation, where they would encounter all the tissues. The nanoparticles must have a hydrodynamic diameter larger than 10 nm to avoid rapid clearance from the body via renal filtration and urinary excretion. Extravasation from the bloodstream poses a significant challenge to nanoparticle delivery to many tissues. Molecules larger than 5 nm in diameter cannot readily cross the capillary endothelium and, therefore, will remain in the circulation until they are cleared from the body [9]. However, there are certain tissues, including the liver, spleen, and tumor, that allow the passage of molecules up to 200 nm in diameter (**Figure. 1.1b**) [10]. After crossing the vascular endothelial barrier and gaining access to the target cells, the nanoparticles have to

face a series of physical barriers. Macromolecules such as siRNA cannot cross the cell membrane easily owing to its relatively large size and high negative charge content. NPs, especially with ligand, can bind and trigger endocytosis to cross the cell membrane and enter into their action site— cytoplasm (**Figure. 1.1c**). More importantly, NPs must escape the endosome (**Figure. 1.1d**); if they do not, they will traffic through the endomembrane compartments of decreasing pH and finally be subjected to degradative conditions in the lysosomes [11]. Finally, encapsulated drugs must dissociate from the delivery carrier and be released to be bioavailable (**Figure. 1.1e**).

The RES is a component of the immune system, which utilizes circulating macrophages, monocytes, liver Kupffer cells, spleen and other lymphatic vessels to remove foreign material, such as bacteria and viruses, from the body. Because bacteria and viruses have the same negative surface charge as phagocytic cells, opsonins are critical to reducing the charge repulsion between the two systems. Phagocytic cells engulf the foreign material once the charge repulsion has been reduced, and transport it to the liver or spleen for further degradation and excretion. Additional phagocytic macrophages are permanently located in the liver, known as Kupffer cells. These cells serve as a major "first pass" filter for many types of NPs and interfere significantly with long circulating time.
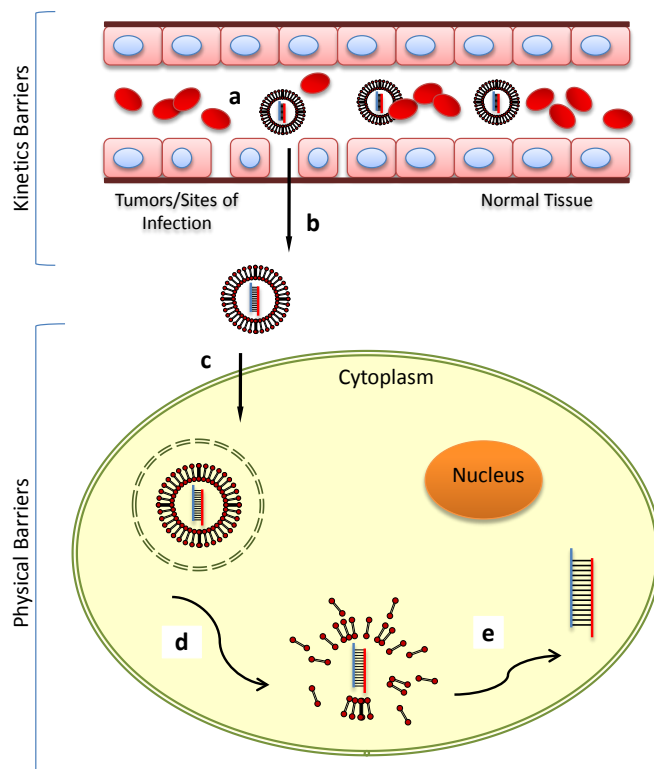
Figure 1.1 Kinetic and physical barriers to the systemic delivered nanoparticle formulation.

(a) NPs should avoid filtration, degradation and RES uptake in circulation; (b) across the vascular endothelial barrier; (c) be internalized into the cells; (d) escape the endosome; (e) disassemble and release the cargo.

1.2   FACTORS AFFECTING PK AND BIODISTRIBUTION OF THE NP

The biological performance of intravenously injected nanoparticles (PK, tissue distribution, therapeutic efficacy and toxicities) is controlled by a complex array of

4

interrelated physicochemical and biological factors. Biological determinants include the biochemical, anatomical, and immunological barriers, as well as the opportunities offered by disease sites for nanoparticlate therapeutics, as described in sections **1.1** and **1.2.1**. The influential physicochemical factors include, but are not limited to the size distribution of NPs, the particles' surface characteristics, particle rigidity, and molecular architecture. These factors are all tunable parameters and could interact with biological barriers *in vivo*. Indeed, a detailed knowledge of particle characteristics would be vital for design optimization.

1.2.1   Effect of size

On the basis of physiological parameters such as hepatic fenestrae, blood vessel extravasation and kidney excretion, it is now well accepted that particle size is a key factor in determining the biodistribution of long-circulating NPs and achieving therapeutic efficacy. The hydrodynamic diameter of a NP is inversely related to its renal clearance. Particles with a hydrodynamic diameter smaller than 6 nm are rapidly cleared by the kidney; an increase in particle diameter can significantly increase the half-life of these particles in the blood. Additionly , the interaction between NPs and RES in the liver and spleen also plays a critical role in nanoparticle clearance. Clearance from the RES depends not only on particle size but also on surface modification, which will be discussed in section **1.2.2**. Current studies suggest that the size of NPs have a substantial effect on protein absorption [12]. Therefore, the PK and biodistribution profiles vary significantly among NPs of different sizes. Nevertheless, it has been consistently shown that PEGylated NPs smaller than 100 nm have

reduced plasma protein adsorption on their surface and a reduced amount of RES uptake [13].

The limited pore size of the endothelial wall in the tissue is the primary delivery barrier for NPs but also provides the opportunity for selective accumulation in certain tissues. Unlike small molecule drugs that can penetrate through the capillary wall into the tissue by passive diffusion, NPs rely on a discontinuous endothelium to pass through the barrier. The major pathway of extravasation of nanoparticles is through leaky blood vessels with increased permeability. Tissues with leaky endothelial walls, including tumors, the liver, spleen, and bone marrow, usually have an increased uptake of NPs. A NP diameter less than 100 nm is required for entry into the hepatocytes due to the presence of fenestrae in the liver sinusoidal endothelium, which have an average diameter of 100 nm [14, 15]. Relatively larger particles (100-200 nm) accumulate in the tumor site through the enhanced EPR effect [16]. Tumor endothelium is often disorganized and does not have a basement membrane. Nanoparticles can penetrate into the tumor parenchyma and be retained, a phenomenon that can be at least partially explained by the lack of lymphatic drainage in the tumor [16]. However, the degree of leakiness of the tumor endothelium, and consequently the optimal size of the nanoparticles, varies significantly among different tumor types [17]. For example, the vasculatures in human brain, pancreatic and ovarian cancers are known to be less leaky than those of other cancers [18, 19].

1.2.2   Effect of surface characteristics

Opsonization is the major factor that induces RES uptake of NPs. However, the surface characteristics of the NPs can counteract the hydrophobic and electrostatic interactions between the NPs and the plasma proteins or macrophages, resulting in less RES uptake and a prolonged blood circulation time. Therefore, surface characteristics of NPs greatly influence their PK and biodistribution. NPs that have a mean diameter of approximately 100 nm with a neutral and hydrophilic polymer-modified surface generally exhibit a prolonged blood circulation and an increased level of tumor delivery.

1.2.2.1 Effect of surface chemistry

It has been reported that surface charge is a very important factor in determining the *in vivo* fate of NPs, as well as the mechanism of cellular uptake and resulting efficiency [20, 21]. Surface charge is usually introduced onto certain types of NPs (such as iron oxide and gold) to improve stability and prevent further aggregation of the particles in aqueous solution via the electrostatic repulsion [22]. However, the optimum surface charges (i.e. positive, neutral or negative) and charge densities, which may prolong the blood circulation time and minimize the nonspecific and undesired distribution of NPs, vary significantly among different nanoparticle systems. These variations might be attributed to the nature of charged groups, the difference in stability of the NPs, and other confounding factors such as particle sizes that are not uniform. A correlation between surface charge (typically net positive) and opsonization has been demonstrated *in vitro* [23]. Therefore, charge shielding is commonly

7

employed through the introduction of surface coatings in order to reduce opsonization. PEGylation technology has been developed to improve the stability, blood circulation time and pharmacokinetics of biopharmaceutical agents. A coating of PEG on the surface of NPs has been shown to prevent particle aggregation and reduce the opsonization with serum proteins, leading to decreased RES uptake and prolonged circulation time [24-26].

Although NPs carrying a negative charge may have significantly less non-specific uptake in the liver and spleen compared with their positive or neutral counterparts, the electrostatic repulsion between negatively charged NPs and cellular surfaces could prevent cellular uptake [27, 28]. Many macromolecules cannot easily cross the cell membrane owing to their relatively large size and high, negative charge content. Extracellular release is not a good design for the delivery of membrane impermeable drugs such as siRNA and proteins. This problem might be solved through the creation of NPs with targeting ligands, which can bind and trigger endocytosis to cross the cell membrane and enter into their action site.

1.2.2.2 Effect of active targeting

It is widely believed that targeted drug delivery using NPs has the potential to provide safer and more effective therapies for oncology applications. Passive tumor targeting takes advantage of the leakiness of tumor vasculature to allow nanoparticle extravasation and accumulation in the tumor site (termed as EPR effect). On the other hand, active targeting exploits the overexpression of surface receptors on cancer cells by providing targeting ligands that can engage these receptors. Current studies on active targeting have used an assortment of ligands ranging from proteins (monoclonal antibodies [29] and their fragments

[30]), nucleic acids (i.e. aptamers [31]), and small molecules (e.g. folic acid [32] and RGD peptide [33]); the attachment of a targeting moiety on the surface of nanoparticles improves their therapeutic outcomes *in vivo* [34]. However, recent work in understanding the parameters that influence targeted nanoparticle behavior has revealed that the presence of the targeting ligand does not significantly affect their PK or biodistribution profiles [35-37]. It is suggested that the enhanced therapeutic efficacy was attributed to the increased cellular uptake of the targeted nanoparticles [36]. Active targeting leads to selective nanoparticle internalization into cancer cells that have abundant receptor expression. Furthermore, these studies also indicate that there is a minimum density requirement of targeting ligand content on the nanoparticle that provides adequate avidity for effective active targeting.

1.2.3   Other factors

Other than the topics discussed above, there are several other critical issues that need to be considered in achieving desired PK and biodistribution patterns. For example, stability is a key issue in the creation of successful pharmaceutical products. The *in vivo* stability is an important prerequisite parameter needed to allow prolonged blood circulation and the preferred tissue distribution.

Shape is another fundamental property of NPs that may be critically important for their intended biological functions. Discher et al. (year) have developed worm-shaped nanoparticles composed of a diblock copolymers, which can circulate in the blood of mice with a surprisingly long half-life (i.e., 5 days) [38]. Park et al. (year) also observed that magnetic nanoworms have a long half-life *in vivo* [39]. Length and flexibility of these

9

particles may also contribute to their long circulation times. Additionally, studies utilizing cultured macrophages revealed that the worm-shaped nanoparticles experience a strong drag force exerted by the fluid flow, enabling them to be carried away by the flow before the macrophages can engulf them. This phenomenon is probably the underlying mechanism of the nanoworms' extremely prolonged circulation time. Mathematical models have been developed to study the adhesion properties for NPs of various shapes; Decuzzi and Ferrari (year) concluded that NPs used for drug delivery should have a radius smaller than 100 nm in order to facilitate their interaction with the endothelium wall [40].

1.3   PEGYLATION: GRAFTING DENSITY AND CONFORMATION

The success of PEGylation critically depends on the steric stabilization conferred by PEG chains on the surface of the NPs. Stabilization is achieved through the highly hydrophilic and flexible nature of PEG chains, which provide repulsive interactions with biological components *in vivo.* The ways in which grafted PEG forms a well hydrated barrier layer on the surface, sterically hindering protein adsorption, can be described by relatively straightforward theories of polymer physics that originated from Flory [41] and De Gennes [42]. Surface-grafted PEG adopts two different statistical conformations, "mushroom" and "brush," that are dictated by the relationship between the distance of two grafting sites and the radius of the random coil the polymer forms in solution. The brush configuration is favored for drug delivery because it ensures that the entire surface of the NP is covered, leaving few gaps where opsonin proteins can freely penetrate and bind [25, 43]. Many studies

indicate that PEG chains must have a minimum molecular weight of 2000 to achieve RES-avoidance, making PEG_{2000} the most frequently used PEG polymer [13, 25, 26]. Essentially, the grafting density of PEG chains determines the efficiency of PEGylation and thereby the protein repelling capability of the resultant NPs.

1.3.1 Steric stabilization by PEGylation

The mechanism by which PEGylation increases circulation times and improves biodistribution profiles is not fully understood. However, the most widely accepted explanation is that PEG provides a steric barrier, which prevents nanoparticle opsonization, which delays removal by the RES. PEGylation involves physical, chemical, and biological stabilization of the liposomes and retention of their payload. The conformational flexibility and high chain mobility of PEG lead to extensive hydration in aqueous environments, causing a steric hindrance to protein adsorption. Thus, such polymers shield the hydrophobic surface of the particles and thereby reduce opsonization by blood proteins and uptake by macrophages of the RES.

In addition to clearance by the RES, aggregation caused by NP-NP interactions may also lead to poor *in vivo* performance. NPs with a high surface energy have a greater tendency to aggregate, primarily because the attraction between particles is stronger than their attraction to the solvent [44]. The interaction potential of spherical NPs is related to their electrostatic repulsive potential and their van der Waals attraction potential. PEGylation decreases the surface energy of NPs and minimizes van der Waals attractions [45].

11

1.3.2   Conformation of surface-grafted PEG

Experimental data closely follows the theoretical model that protein repellence by PEG coatings depends on both length and density of the chain which jointly determine the thickness of the PEG corona. The conformation of surface grafted PEG chains is dictated by the relation between the distance of two grafting sites (D) and the radius of the random coil the polymer forms in solution (R_F), the latter being defined by the Flory dimension ($R_F = aN^{3/5}$), where N is the degree of polymerization and a is the monomer size [46]. The polymer forms a mushroom conformation at $D > 2R_F$, while a brush-like conformation appears at $D < R_F$, when the polymer chains stretch out perpendicularly from the surface due to steric hindrance among each other (**Figure 1.2a**).   These two conformations do not represent sharply separated regimes, but undergo smooth transitions through mushroom/brush intermediates as D and R_F values became closer [47]. The transition between the mushroom and brush regimes occurs at the concentration of grafted PEG-lipids (X_{m-b}) where the PEG chain first begins to overlap as random coils (i.e. mushroom).   This concentration is determined by the size of the polymer (R_F).

An increase in PEG:mole fraction or density can lead to a significant increase in the circulation half-life of the NPs, a consequence of reduced protein binding and opsonization [26]. However, PEG–lipid conjugates are detergent-like surfactants which tend to form mixed micelles with other lipids, thus they can only stably incorporate as a small mole-fraction of any lipid membrane [48-50].   In this low mole-fraction (usually less than 5 mol%), the polymer chains adopt a mushroom conformation. Density and thickness of the PEG corona cannot provide full protection of the hydrophobic surface from opsonization, as

shown in Figure 1.2a. Li & Huang employed PEGylated liposome-polycation-DNA (LPD) NPs to address this issue (citation). In that formulation, the nucleic acid was complexed by protamine to form a compact core, which was coated by two cationic lipid-bilayers. The inner bilayer is directly in contact with the core and is supported and stabilized by the charge-charge interaction of the cationic lipids with the negatively charged core. This unique feature of LPD may enable the supported bilayer to tolerate a high amount of DSPE-PEG$_{2000}$ (10 mol %), forming a relatively dense PEG brush on the surface [51]. As a result, the zeta potential of an unprotected LPD is +40 mV, while a fully protected LPD contained 10 mol% surface-grafted PEG has a zeta potential of approximately 0 mV. LPD containing 10 mol% PEG was not taken up by the liver Kupffer cells, thus completely evading the RES [52, 53]. Of course, the accumulation in the tumor still depends on how leaky the tumor vasculature is, i.e., the EPR effect.

Our recent studies also showed that small nanoparticles require a higher amount of PEG-lipids to avoid RES uptake (data unpublished). In other words, X_{m-b} (the concentration of grafted PEG-lipid for which the PEG chains first begin to overlap) increases with decreasing particle size. On the surface of a small particle, each PEG-lipid molecule can occupy a larger volume than if it is on a flatter surface (**Figure 1.2b**). This is due to the high curvature of a small particle. Consequently, the PEG chains exert less steric interactions (i.e. excluded volume effects) and tend to appear in the less compact and less dense mushroom conformation. To assure a brush-like conformation of the coating, the amount of PEG-lipid conjugate should be increased. The Flory radius for PEGs of molecular weight 750, 2000 and 5000 is R_F = 2.1, 3.8 and 6.7 nm, respectively [46]. Since the size of commonly used nanoparticles is usually around or larger than 100nm, the curvature effect is of little

significance. As the particle size decreases, its influence will need to be taken into consideration. X_{m-b} will be determined by the size of PEG-lipids (R_F) as well as the radius (r) of the nanoparticle on which they are grafted.
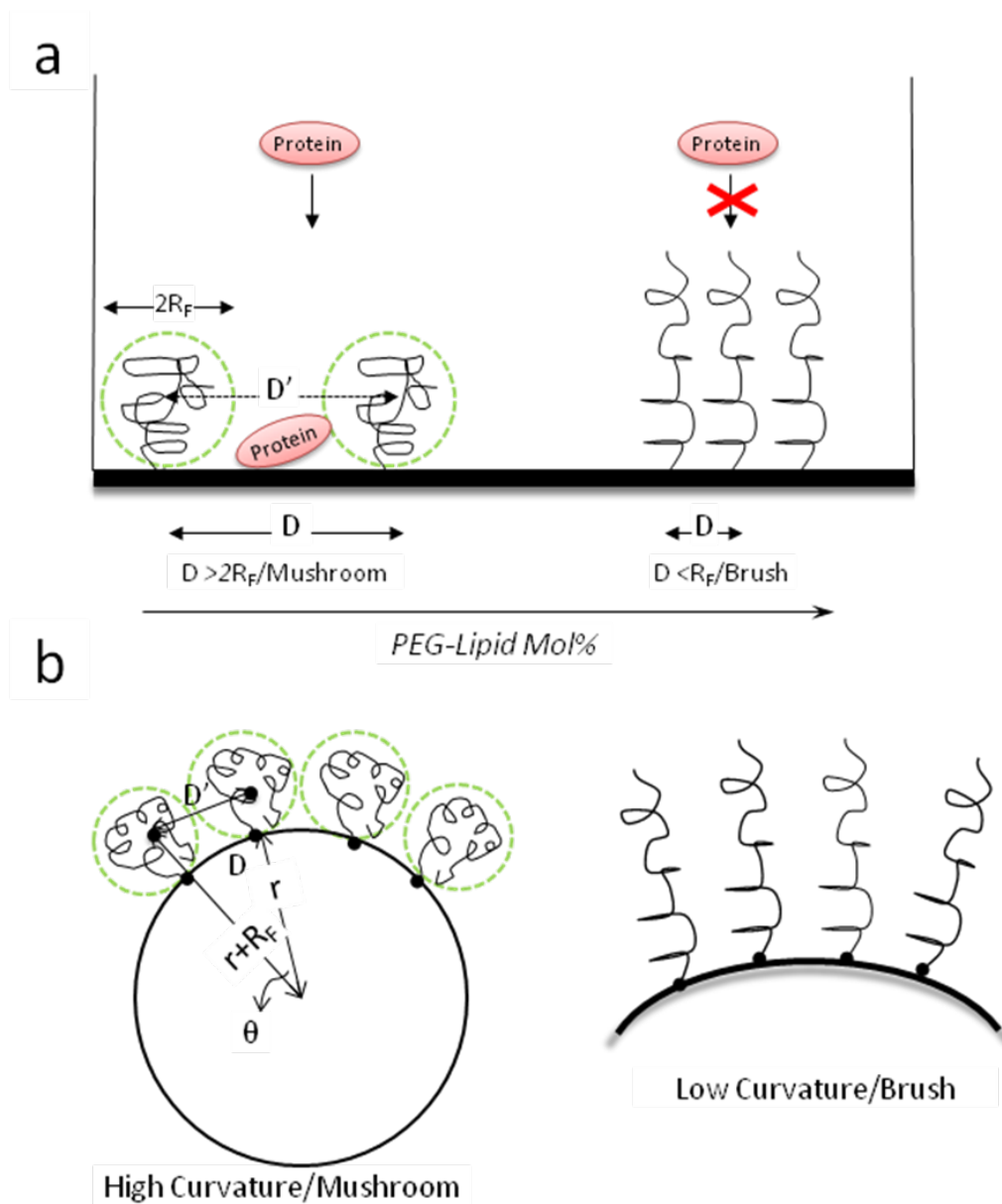
Figure 1.2 Putative PEG conformation regimes with respect to the polymer concentration in (a) the bilayer and (b) the curvature of the bilayer.

1.3.3 Linkage of PEG to NPs

Both covalent and noncovalent approaches are used to anneal PEG molecules to the NP surface. In the creation of solid NPs, such as gold NPs, a thiol group is the classic approach. Here, a sulfhydryl-capped PEG chain adheres to the gold surface [54]. Silica NP surfaces are generally capped with an organosilane such as amino- or mercapto-trimethoxysilane for routine bioconjugation [55].

A commonly used approach in noncovalent PEGylation involves coating the hydrophobic NP surface with lipid–PEG conjugates through hydrophobic interactions. For example, to prepare PEGylated liposomes, it is feasible to simply include PEGylated lipids into the lipid mixture, or incubate naked liposomes with aqueous micellar solution of lipid–PEG conjugates [56]. PEGylated phospholipids are able to bind to the hydrophobic surface of NPs, for example single-walled carbon nanotubes [57], hydrophobic polymeric NPs [58], or quantum dots [59], in such a way that hydrophilic PEG groups are facing the aqueous exterior and provide the nanotubes with a hydrophilic PEG corona. The hydrophobic interactions between lipids and NPs anchor the PEG chain.

1.3.4 Coverage density and conformational studies

PEG density on the nanoparticle surface has been found to be a critical factor in modulate nanoparticle behavior *in vivo* and in nonspecific cellular uptake. To date, there is no direct method available for quantifying the number of PEG molecules bound to a NP surface or for determining the density of PEG [60]. Many reports simply assume a complete

loading of added PEG molecules to determine the density. Thus, the exact influence of PEG-density dependence on NP biodistribution remains unknown.

Dynamic light scattering reveals three important characteristics of the final PEGylated NPs: size, zeta potential and size distribution. Size measurement by dynamic light scattering suffers from poor reproducibility, yet it is convenient and can be used to monitor the sequential size increases which occur before and after PEGylation [61]. The size distribution can be used to measure the homogeneity of the NPs. Although size increases offer some evidence of PEGylation, it cannot discriminate between brush and mushroom configurations. Zeta potential also offers information regarding the surface coating; reduced surface charge may indicated the presence of PEGylation. Unfortunately, these measurements are suboptimal and inconclusive in determining PEG density and conformation.

Raman analysis offers detailed information on concentration and conformation, but is generally beyond the scope of most laboratories [62]. Nuclear magnetic resonance (NMR) is a method that is more widely available and is used to detect the ethylene protons at 3.65 parts per million, but it is not quantitative [63]. Alternatively, thermal gravity analysis (TGA) has also been used to estimate the number of PEG chains on the surface of a nanoparticle. It measures the mass change before and after removal of PEG chains by using thermal desorption and decomposition. To measure the mass loss accurately, a relatively large quantity of the sample is required. The coverage density calculated from TGA data corresponds to the total number of PEG chains in the sample, including those loosely trapped among the particles. Some groups, including ours, have successfully used fluorescence-

labeled PEG to model the binding densities possible at different density levels. This approach may not be appropriate for gold NPs because of quenching.

NPs that have a PEG corona adopt a core-shell structure, concentric domains of two chemically different materials, a structure that is ubiquitous in the colloid science field. Structural information on core-shell systems can be assessed effectively using scattering techniques. In particular, they can be studied in great detail using contrast-variation methods [64], achieved most readily in the context of small-angle neutron scattering (SANS). Several studies have also used light or X-ray scattering. In this work, we use SANS to investigate the aqueous dispersions of PEG-grafted, LCP NPs under two different temperatures. We focus on how the signals change in relation to increasing temperature. The conformation of grafted-PEG could be estimated by model fitting the signals. Detailed information of SANS studies is provided in APPENDIX A.

1.4   PROTEIN ADSORPTION ONTO NANOPARTICLES

1.4.1   Formation of the protein corona

In comparison to bulk biomaterials, NPs have an extremely high surface-to-volume ratio. Control of this, as well as other surface properties, is crucial to the *in vivo* performance of NPs. It is now well-recognized that the surfaces of NPs are immediately covered by proteins when they come into contact with a biological medium [65, 66]. The absorption of proteins to such surfaces confers a new "biological identity" to NPs in the biological milieu, which is what cells, tissues and organs actually "see" when interacting with NPs [67]. This

new "bio-nano interface," created by covering NPs with a complex layer of proteins (corona), determines the subsequent cellular/tissue responses and biological consequences [68, 69]. Surface characteristics such as charge, hydrophilicity and curvature dictate the extent and specificity of protein binding [67, 70]. Specific protein binding is one of the key elements that affect biodistribution of the NPs. Indeed, a detailed knowledge of NP-protein interaction is vital for a rational formulation design as well as optimization.

1.4.2   Analytical method for corona evaluation

Analysis of the protein corona involves purification of protein-NP complexes and separation and identification of the purified proteins. To date, the routine method for isolating protein-NP complexes is centrifugation. Relative to other techniques, centrifugation is easy and requires little material. Separation by centrifugation has been used to identify major plasma proteins such as human serum albumin (HSA), immunoglobulins, and fibrinogen bound to the NPs [66], [71]. It is not surprising to find these proteins bound to injected NPs because these are some of the most abundant proteins found in human plasma.

A common technique for the separation of the proteins is one or two-dimensional polyacrylamide gel electrophoresis (1D- or 2D-PAGE). To identify individual proteins, it is common practice to conduct mass spectrometry followed by peptide sequencing on individual excised protein spots from the 1D or 2D gel and compared to a known database of proteins [72]. For the identification of particular proteins of interest, immunoblotting and Western blotting have also been applied [73].

Aside from gel electrophoresis, other separation methods involving gel filtration, such as size-exclusion chromatography or affinity chromatography, are also used to separate proteins from plasma and identify individual proteins [66].

1.4.3 Outcome of protein-NP interactions

While the complete plasma proteome is expected to contain as many as 3700 proteins [69], of which only approximately 50 have been found in the protein corona associated with nanoparticles [67, 74]. Specific protein binding can have a direct effect on biodistribution and internalization of NPs. Certain components of the corona proteins allow macrophages of the RES to easily recognize NPs. These proteins are knownas "opsonins." Binding of opsonins, for example, fibrinogen, Immunoglobulin G (IgG), and complement factors, are believed to promote phagocytosis and the removal of the particles from systemic circulation via cells of the RES. These particles tend to sequester in the RES organs very rapidly and concentrate in the liver and spleen. On the other hand, dysopsonins such as HSA generally prolong circulating time in the blood [75].

Apolipoprotein adsorption has been reported with various NPs. Its biological significance presumably depends on the conformation of apolipoproteins and the exposure of functional motifs that may serve as ligands for lipoprotein and scavenger receptors expressed by macrophages, hepatocytes and vascular endothelial cells [76, 77]. It was reported that specific apoE binding to NPs may facilitate delivery across the blood brain barrier (BBB) into the brain, and the adsorption of apolipoproteins has been shown to be important for the

transportation of drugs across the BBB and into the brain, though the mechanism of transport is still under debate [78].

To inhibit opsonization and subsequent clearance by the RES, the surface of the NPs can be coated by hydrophilic polymers such as PEG to reduce protein binding [79-83]. The mechanism by which PEG decreases protein interactions is non-specific [84]. PEG is not the only polymer that can be attached to NPs to inhibit the protein binding to the surface of the NPs and avoid immune recognition. Various other polymers and polysaccharides have been utilized in place of PEG. In all cases, protein adsorption was not completely avoided (i.e. HSA, fibrinogen, IgG, and apolipoproteins were detected), but was greatly reduced [72].

1.5   PERSPECTIVES OF OPTIMIZING IN VIVO PERFORMANCE OF NP

Outcomes from studies completed in the past decade regarding the biological responses to nanomaterials have greatly influenced design of nanoparticle therapeutics. Material design evolved whenever the effect of size, shape, or surface chemistry was further elucidated. Currently, the engineering of NPs for biomedical applications has been focused on novel nanomaterials functionalized with optimized surface chemistries that improve stability, bioavailability and biocompatibility. This approach, however, has encountered certain limitations. First, there appears to be an overreliance on the EPR effect to deliver NPs into tumors, when the efficacy of this phenomenon might be highly variable amongst different tumors and individual patients. Second, there is no single property of NPs that can be optimized to ensure efficient delivery, as NPs have to travel through multiple, distinct barriers in the body.

Responding to these limitations, researchers recently shifted the paradigm of design from stable nanomaterials to "environment-responsive" systems that possess stimuli-responsive properties. External stimuli cause changes in the particle size, shape or surface structure, and lead to their rearrangement to improve targeted compound delivery. These dynamic nanoparticle systems may use biological, physical, or chemical factors in their target environment to trigger a change in their properties to maximize targeted delivery. Two approaches have been used so far. The first uses hallmark cues inside the target environment such as low pH, low O_2 and ormatrixmetalloproteinase enzymatic activity within the tumor. One example is NPs with a PEG surface layer that will shed off in response to pH to reveal a positively charged surface. These particles target and are retained in hypoxic tumor regions [85]. Other groups have used pH to trigger the breakdown of the NPs to release drugs in local tumor environment [86]. Enzymatic activity has also been used as a trigger for drug release [87]. Additionally, by using local cues inside the tumor to trigger drug release, the NPs localized in the liver and spleen do not cause toxicity.

Alternatively, a multistage nanoparticle delivery system was designed with the ability to change size, triggered by proteases that are highly expressed in the tumor microenvironment (e.g. matrix metalloproteinases (MMP)). The enzyme degrades the cores of 100 nm gelatin NPs, releasing smaller 10 nm quantum dots from their surface. The rationale of this design lies in that many of the current nanotherapeutics are designed to be around 100 nm in diameter to exhibit enhanced accumulation around the leaky vasculature in the tumor. Their large size, however, hinders penetration through the dense extracellular matrix. Therefore, a multistage system in which 100 nm NPs "shrink" to 10 nm NPs after they extravasate from leaky regions of the tumor vasculature and are exposed to the MMP-2

21

in tumor microenvironment maximizes tumor delivery. The shrunken NPs can more readily diffuse throughout the tumor for improved diagnostic sensitivity [88]. The second approach applies an artificial environmental cue such as near-infrared (NIR) light upon the target tissue. The NIR light can excite gold nanorods or nanoshells inside the tumor to generate heat to trigger localized drug release from the liposomes [89, 90].

Recently, inspired by the ability of communication to improve targeting in biological systems (e.g. inflammatory-cell recruitment to sites of disease), the concept of "communicating nanoparticles" was broached. The "locator particle" is a gold nanorod, which extravasates through the abnormally large pores of tumor blood vessels. Subsequently, infrared light is applied to heat up enough to initiate the coagulation cascade. Here, the "receiver particle", which is designed to target specific molecules produced by the coagulation process at a high concentration, comes into play. In this way, the "locator particle" broadcasts tumor location to the clot-targeted "receiver particle" in circulation, thereby amplifying the tumor delivery of both. This approach does not overly rely on the EPR effect and can deliver doses of chemotherapeutics to tumors that are over 40 times higher than those delivered by non-communicating controls [91].

CHAPTER 2

METHODOLOGY FOR PK / BIODISTRIBUTION STUDIES

The biodistribution of LCP NPs in tumor-bearing mice was investigated using fluorescence imaging. A quantitative validation of this method was done using ^{3}H and ^{111}In to label the nanoparticles. The biodistribution of LCP NPs containing oligonucleotides was investigated using three different probes: Texas-Red labeled oligonucleotides, ^{3}H-labeled oligonucleotides, and ^{111}In-labled calcium phosphate. A discrepancy was found between the radioactivity and the fluorescence signals. Signals from ^{3}H and ^{111}In exhibited very similar distribution patterns, suggesting that the liver and spleen were the major accumulation sites. However, fluorescence imaging indicated that tumor accumulation was predominant. We confirmed that the fluorescence signals in both liver and spleen were less than those in the tumor due to the intrinsic tissue absorption and scattering. The use of NIR dye Cy5.5 brings about the same problem, in that the quantitative data from whole organs was dramatically affected by the absorption and scattering properties of the tissue. Careful attention must be paid to the quantification and interpretation of fluorescence imaging measurements when comparing different tissues. The following PK and biodistribution studies were performed using LCP NPs containing ^{3}H-labeled oligonucleotides.

2.1   INTRODUCTION

The use of therapeutic macromolecules such as oligonucleotides has been intensively studied for the treatment of several major disorders. A key issue in the successful development of these therapies is to understand and control the biodistribution of macromolecules [92]. PK and biodistribution studies can provide invaluable information early in the development. This importance has created a need for techniques that can analyze the macromolecules qualitatively. Traditionally, biodistribution studies of macromolecules were carried out in animals by measuring the radioactivity associated with the drugs [93, 94]. Mass spectrometry methods have also been developed to study the biodistribution of drugs, which allows for both quantification and identification of the analyte [95]. Obviously, radioactive compounds are a potential health hazard and environmentally unfriendly. Synthesis and disposal of radioactive compounds are expensive. For some isotopes with relatively short half-lives, radioactivity decay is quite rapid and thus, the compounds lose their usefulness in time. Mass spectrometry (MS) is now playing a central role in PK and biodistribution studies. Advances in ionization methods, including electrospray ionization (ESI) and matrix-assisted laser desorption/ionization (MALDI), have expanded the use of MS in investigating macromolecular drugs. However, successful MS measurement relies on target molecule extraction/isolation from biological specimens, which can be complicated [96]. Many labs still cannot readily access the resources and expertise required for this

method. In addition, mass spectrometry is an end-point measurement, which lacks the ability to probe dynamic events in real time.

Due to the aforementioned circumstances, fluorescence imaging is emerging as a popular modality to couple with the traditional methods. Fluorescent dyes are conjugated to the drug to produce optical probes used *in vivo* or *ex vivo*. This technology is relatively safe, low-cost and noninvasive. The key to effective imaging, especially in deep tissues, is the use of fluorophores with a red or NIR emission range (600–1000 nm), which corresponds to low photon absorption and auto-fluorescence in tissues. Biological chromophores, in particular hemoglobin, strongly absorb visible light, thereby limiting the penetration depth to only a few millimeters. Other biological components, such as water and lipids, are optically transparent from the visible to the NIR range, but strongly absorb light in the infrared. The combined absorption of these components translates into an optical imaging window of approximately 600 to 1000 nm where the absorption coefficient of tissue is at a minimum. Additionally, light scattering and auto-fluorescence are low in the NIR. This allows a significant signal with relatively low background [97, 98].

Many researchers, including ourselves, have used fluorescence imaging to assess the biodistribution of nanoparticles loaded with fluorescence-labeled drugs [99-102]. This method gives an indication of tissue accumulation patterns, which facilitates the design and optimization of the formulation. Although most of these studies quantified the biodistribution based on the fluorescence intensity, the validation of this method in a variety of tissues has not yet been studied systematically. Here, we investigated the biodistribution of LCP NPs containing oligonucleotides using three different probes: 1) Texas Red labeled oligonucleotides; 2) ^{3}H-labeled oligonucleotides; and 3) ^{111}In, which can form co-precipitate with calcium phosphate, and was used as a radiotracer for the intact LCP NPs. LCP contains

an amorphous, calcium-phosphate-precipitate core wrapped with a single lipid-bilayer with surface modification of polyethylene glycol with and without a targeting ligand [99]. The NP formulation has been successfully used to deliver siRNA [99, 103] and cDNA (unpublished results) to both solid and metastatic tumors. Our results showed a discrepancy between the radioactivity and the fluorescence signals. Signals from ^{3}H and ^{111}In exhibit very similar distribution patterns, suggesting that the liver and spleen were the major accumulation sites. However, fluorescence imaging indicated that tumor accumulation was predominant. Furthermore, we found that the fluorescence signals in both liver and spleen are greatly attenuated compared with those in the tumor due to the intrinsic tissue absorption and light scattering. Therefore, careful attention must be paid to the quantification and interpretation of fluorescence imaging measurements, which could skew the data towards the tissues with less light absorption and scattering.

2.2   MATERIALS AND METHODS

2.2.1   Materials

22-mer oligonucleotides (sense sequence, 5'-CAAGGGACTGGAAGGCTGGG-3',) labeled with Texas Red or Cy5.5 Dye (excitation/emission wavelengths of 550/600 nm and 650/700nm, respectively), were purchased from Sigma, Inc. Both Texas Red and ^{3}H-labeled oligonucleotides were used to mimic siRNA. Dioleoylphosphatidylcholine (DOPC), dioleoylphosphatydic acid (DOPA), 1,2-distearoyl-sn-glycero-3-phosphoethanolamine-N-[poly(ethylene glycol)2000] (DSPE-PEG$_{2000}$) were purchased from Avanti Polar Lipids, Inc.

(Alabaster, AL). NCI-H460 human lung cancer cells were obtained from American Type Culture Collection.

2.2.2 Experimental animals

All animal work was performed in accordance with and approved by the University of North Carolina Institutional Animal Care and Use Committee guidelines. Athymic nude (nu/nu) mice carrying H460 human lung cancer xenografts were used for all of the experiments.

2.2.3 ^{3}H labeling of oligonucleotides

^{3}H labeling of oligonucleotides was prepared by inducing hydrogen exchange with ^{3}H$_2$O at the C8 positions of purine oligonucleotides using methodologies described by Graham et al. [104]. For each labeling experiment, 12 mg of 22-mer oligonucleotide was dissolved in 200 μL of 50 mM sodium phosphate and 0.1 mM EDTA (pH 7.8) and lyophilized in a 2 mL glass microfuge tube. The dry oligonucleotide was resuspended in 200 μL of ^{3}H$_2$O (Moravek, specific activity 5 Ci/gm) containing 8.3 μL of the free radical scavenger, β-mercaptoethanol. The sample was incubated at 90°C for six hours. Following the incubation, the sample was lyophilized to remove ^{3}H$_2$O that had not been exchanged. The sample was resuspended in 1mL water and allowed to rest at room temperature for one hour to enable the exchangeable protons to dissociate rapidly. The period of incubation at room temperature was followed by four cycles of lyophilization and subsequent resuspension in 0.5 mL of water. The labeled oligonucleotide was then purified using a spinning column

containing Sephadex G-25 (GE Healthcare, Life Sciences). The radiolabeled compound is stable in biological systems and was stored at -20°C for further experiments.

2.2.4 Preparation of LCP NPs

LCP NPs were prepared according to the method described previously with minor modifications [99]. We first prepared two water-in-oil microemulsions: 1) 100 μL of 500 mM $CaCl_2$ and 16 μL of 2 mg/mL Texas Red or ^{3}H-labeled oligonucleotides in 8 mL cyclohexane oil phase (71% cyclohexane with 29% Igepal CO-520 as surfactant) and 2) 100 μL of 100 mM pH 9.0 Na_2HPO_4 also in 8 mL cyclohexane oil phase plus 320 μL of 20 mM DOPA as the inner leaflet lipid. ^{111}In-loaded nanoparticles were created by adding radioactive $InCl_3$ (in 0.05 N HCl, PerkinElmer, Inc.) to the $CaCl_2$ microemulsion, as a sufficient amount of 0.05 N NaOH was added to the Na_2HPO_4 microemulsions to neutralize the acid. After mixing the two solutions for 45 min, 30 mL of absolute ethanol was added to the micro-emulsion and the mixture was centrifuged at 12,500 g for 15 min to precipitate the CaP (or CaP/In) cores. After being washed extensively with ethanol 2–3 times, the pellets were dispersed in 500 μL chloroform and stored in a glass vial for further modification. For outer leaflet lipid coating, 200 μL of 20 mM cholesterol, 200 μL of 20 mM DOPC, and 100 μL of 20 mM of DSPE-PEG$_{2000}$ were mixed with the core. After removal of the chloroform, the core was first suspended in a small volume of ethanol, and then dispersed in an aqueous solution containing 5% dextrose.

2.2.5 Tissue distribution study by Texas Red labeling

LCP NPs containing Texas Red-labeled oligonucleotides were intravenously injected into the tumor-bearing mice at a dose of 0.25 mg/kg of oligonucleotides. Four hours later, mice were sacrificed and tissues of interest were collected for fluorescence imaging. Fluorescent images were acquired under the IVIS Imaging System (Xenogen Imaging Technologies, Alameda, CA) at indicated wavelengths.

2.2.6 Tissue distribution study by radioisotope labeling

A dose of 0.25 mg/kg of oligonucleotides of labeled LCP NPs was intravenously injected into the mice. Four hours later, mice were sacrificed and tissues of interest were collected for further analysis. The amounts of ^{3}H-labeled oligonucleotides and ^{111}In that accumulated in different tissues were quantified using liquid scintillation and gamma counting, respectively.

2.2.7 Fluorescence intensity measurement in different tissues

Un-injected animals were euthanized and their blood was collected using cardiac puncture. The livers, spleens and tumors of these mice were also harvested. To measure the fluorescence intensity in whole organs, 0.25 µg of Texas Red labeled oligonucleotides were directly injected into the livers, spleens and tumors of the mice using a Hamilton syringe. To measure the fluorescence intensity in tissue homogenate, tissue samples were weighed and placed in a homogenization buffer (10 mM Tris pH 7.4 and 0.5% Triton X-100) at a ratio of

100 mg of tissue per mL. One-hundred μL each of blood, tissue homogenate and homogenization buffer were then transferred to a 96 well plate. Ten μL of homogenization buffer containing various amounts of Texas Red oligonucleotides were added. The tissues and plate were then imaged using an IVIS Imaging System as described above. The plate was also measured by a plate reader (Bioscan Inc., Washington DC) for the fluorescence intensity in order to create standard curves.

To prepare the perfused liver, un-injected animals were euthanized and 3 mL of warm PBS was perfused via portal vein through the liver to expel the blood. The perfusion rate was kept at about 3 mL/min. Texas Red-labeled oligonucleotides (0.5 µg) were directly injected into non-perfused liver, perfused liver and tumor, respectively. The tissues were then imaged using the Kodak In Vivo Imaging System FX Pro (Carestream Health, Woodbridge, CT) at indicated wavelengths.

2.2.8   Statistical analysis

Data are presented as the mean ± SD. The statistical significance was determined by using the two-sided student t-test. P values of <0.05 were considered to be significant.
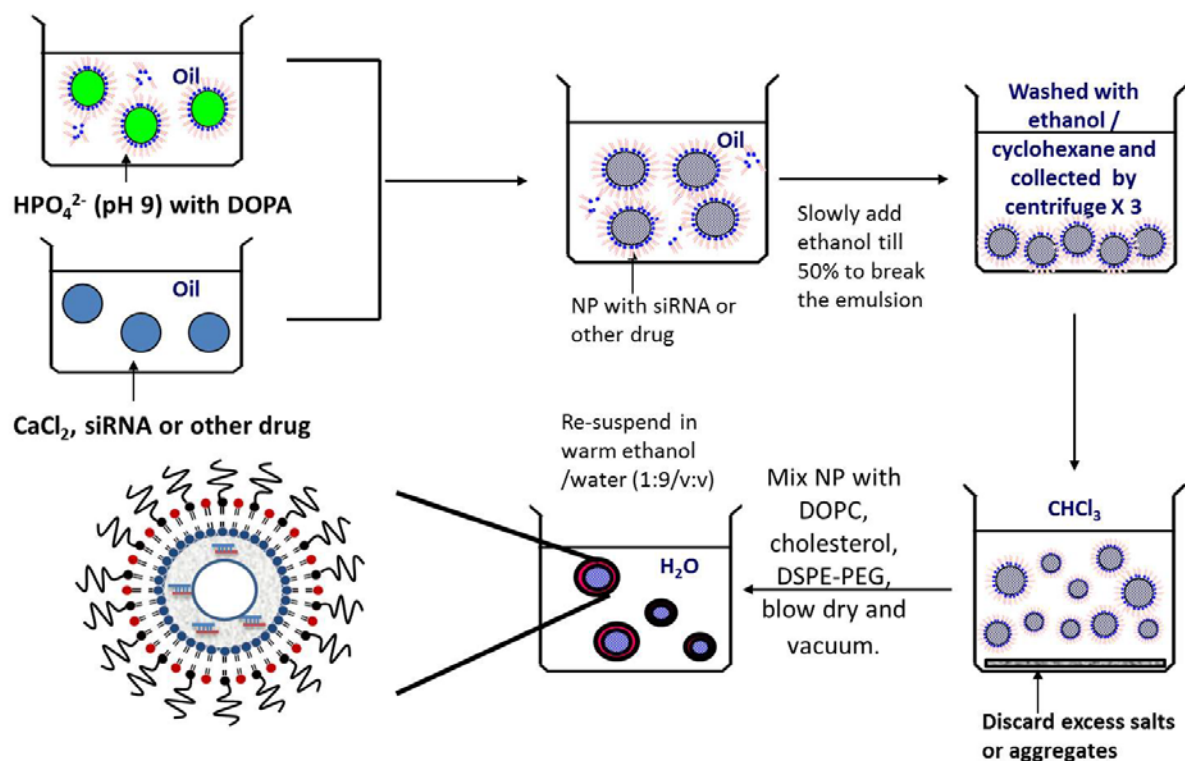
Figure 2.1 Formation of LCP NPs formulation in microemulsion.

2.3   RESULTS

We investigated the biodistribution of LCP NPs in tumor-bearing mice using Texas Red, ^{3}H and ^{111}In labeling. ^{3}H labeling revealed that significant accumulation of the nanoparticles occurred in the liver (30% injected dose (ID)) and the spleen (15% ID), while only 5% ID was found in the tumors (**Figure 2.2A**). Consistent with the ^{3}H data, around 20% ID and 15% ID of ^{111}In were found in the liver and spleen, respectively (**Figure 2.2B**). Less than 5% ID was seen in the tumor. The agreement between the labeling of the drug (^{3}H-oligonucleotides) and that of the drug carrier (^{111}In) suggested that this biodistribution pattern may accurately represent the *in vivo* behavior of LCP NPs. However, as shown in **Figure**

2.2C, significant fluorescent signals could be detected in the tumors, while the brightness of the liver and spleen remained just above the background level. To test whether fluorescence intensity of labeled oligonucleotides is subjected to the microenvironment in which they reside, the liver, spleen and tumors were dissected from un-injected animals and directly injected with fluorescence-labeled oligonucleotides. The *ex vivo* fluorescence imaging is shown in **Figure 2.3A**. Minimal signals were detected in the liver and the spleen. In contrast, the tumor showed significant fluorescence. These results suggested that tissue characteristics in the liver and the spleen strongly influences and reduced the fluorescent signals.

Whole blood and tissue homogenate were then used to study the fluorescent signal linearity and reduction effect in different organs. As **Figure 2.3B** shows, when equal amounts of Texas Red-labeled oligonucleotides were added, the intensities in the tumor homogenates and buffer were higher than those in whole blood, liver and spleen homogenates. By adding 15 μl of whole blood to 100 μl of tumor homogenate, the fluorescent signal was greatly diminished. These results suggested that blood played an important role in reducing the Texas Red signals from tissues, the phenomenon can be explained by the fact that hemoglobin has its secondary absorption peak between 550nm and 600nm. Therefore, the sensitivity of the Texas Red probe could be greatly hampered in blood-enriched tissues such as the liver and spleen. Using the liver perfusion technique, the role of blood hemoglobin in reducing the Texas Red signal was further elucidated. The results are shown in **Figure 2.3C**. As the perfused mouse liver contained less blood, when injected with the same amount of Texas Red-labeled oligonucleotides, it emitted stronger fluorescence than the non-perfused liver. We demonstrated that a similar problem also existed in using a NIR probe. With equal amounts of Cy5.5 dye, the intensities in the tumor homogenate and buffer were higher than those in whole blood and the liver homogenate

(**Figure 2.4**). These differences should be taken into account in the quantitative analysis of biodistribution data. Texas Red-labeled oligonucleotides exhibited reasonable linearity in each tissue homogenate, including the liver, spleen and tumor, but the attenuation coefficient of these tissues (the slopes in **Figure 2.5**) were dramatically different. While quantitative comparison in a tissue-specific manner is valid (e.g. liver vs. liver, tumor vs. tumor), it is not appropriate to measure the accumulated amount of the dose by comparing fluorescence intensity between different tissues.
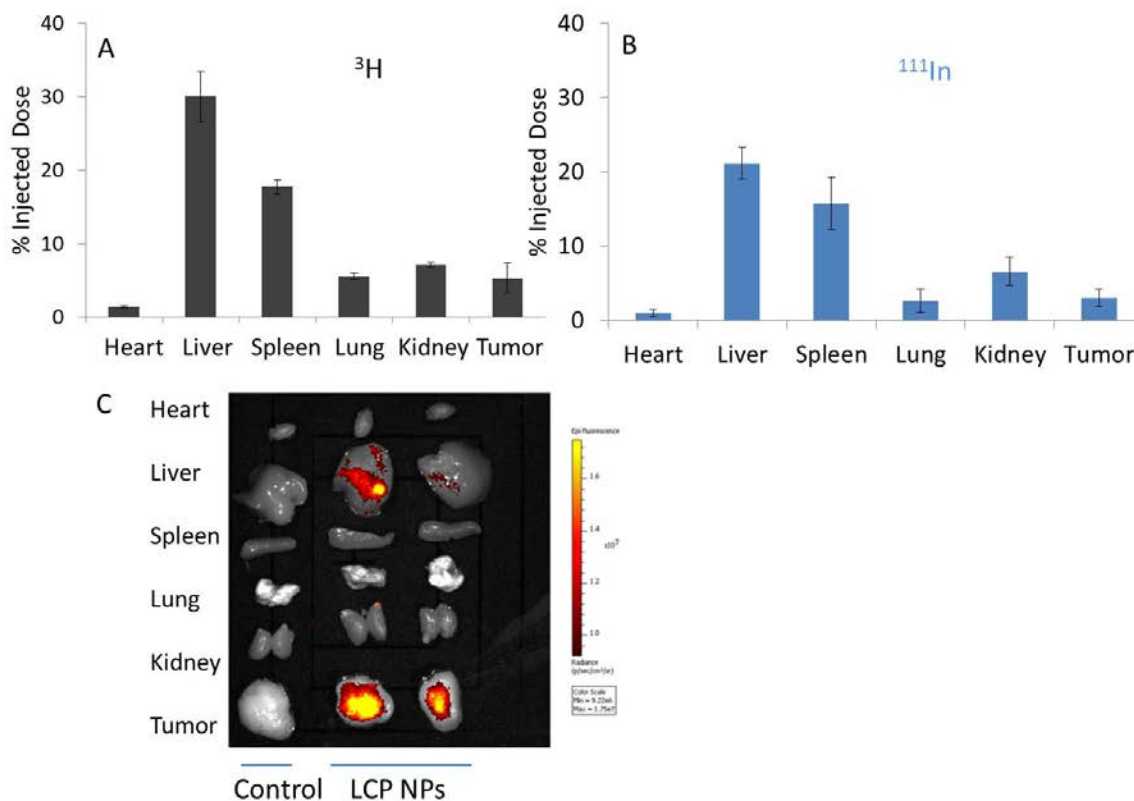
Figure 2.2 Biodistribution of LCP NPs in tumor-bearing mice.

Signals were detected by (A) ^{3}H, (B) ^{111}Indium, and (C) fluorescence (Texas Red) signals.
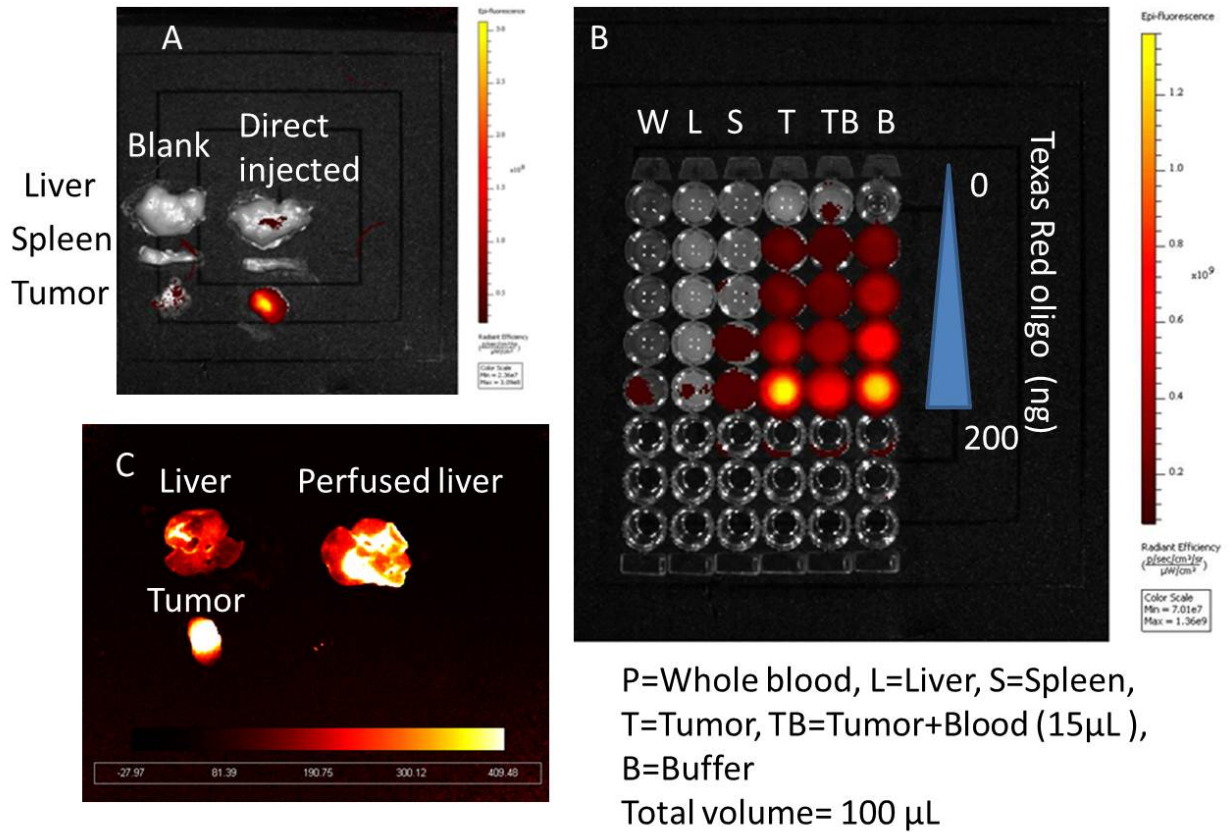
Figure 2.3 Measured fluorescence intensity of Texas Red oligonucleotides.

(A) Texas Red signal in whole organs; (B) Texas Red signal in tissue homogenate; (C) Texas Red signal in non-perfused and perfused liver. (Excitation/emission wavelengths: 550/600 nm).

W=Whole blood, L=Liver, T=Tumor, B=Buffer
Total volume= 100 µL
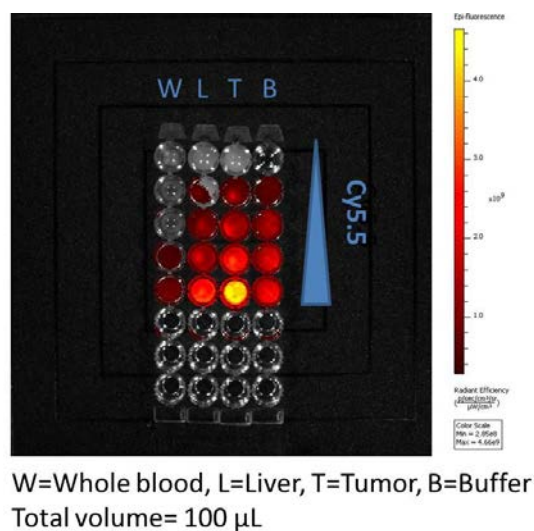
Figure 2.4 Measured fluorescence intensity of Cy5.5 in tissue homogenate.

(Excitation/emission wavelengths: 650/700 nm)

y = 0.4824x
R² = 0.9634

y = 0.9614x
R² = 0.9774

y = 1.5534x
R² = 0.9317

y = 4.6344x
R² = 0.9857
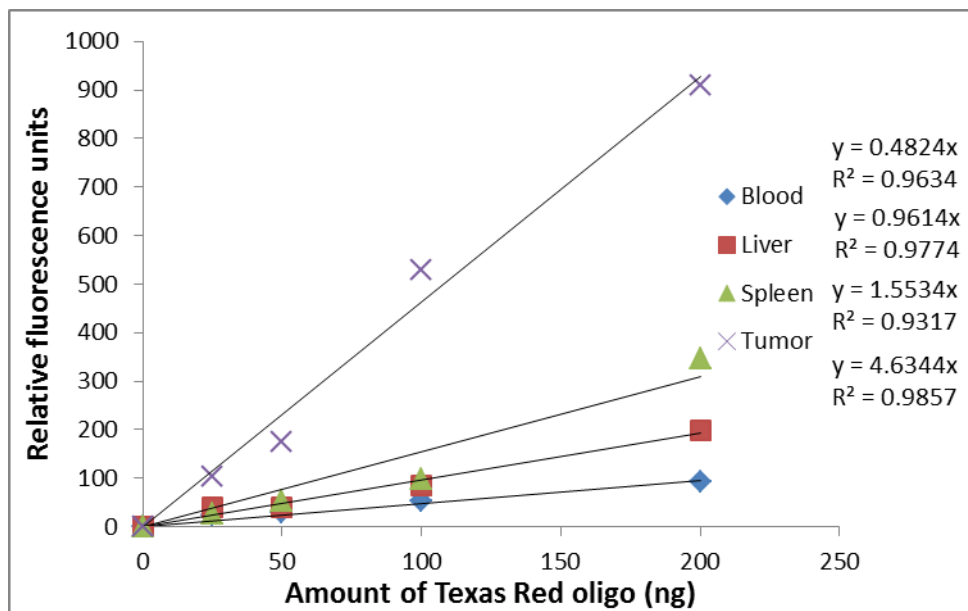
Figure 2.5 Standard curve generated by quantifying the intensities of known concentrations of oligonucleotides.

(Excitation/emission wavelengths: 550/600 nm)

2.4 DISCUSSION

Fluorescence labeling of macromolecules has played a major role in biomedical research. It is desirable because of its high sensitivity, excellent spatial and temporal resolutions, and the capability for multimodality imaging. It extends our ability to track a particular molecular, cellular, or even physiological event using noninvasive visualization and measurement within the *in vivo* context. In spite of the many advantages offered by fluorescence imaging, the technique also presents serious challenges. Some issues regarding the use of fluorescence imaging in different tissues include auto fluorescence, light

absorption, and light scattering. NIR dyes generate less background fluorescence, since auto fluorescence in tissues is mostly excited by near ultraviolet and blue light and emits in the yellow range [105]. Moreover, it has been demonstrated that use of red and NIR probes increases the depth of penetration in mammalian tissues by several orders of magnitude by avoiding the major absorption regions of hemoglobin. However, it is note-worthy that hemoglobin exhibits a broad absorption band. Even though the absorption of hemoglobin is much less intense in the NIR region, its contribution (in particular, by oxyhemoglobin) to the total light attenuation is certainly not negligible for quantitative purposes. Scattering has a weak dependence on wavelength. It arises due to a different relative refractive index at the boundaries between two different structures, such as the extracellular fluid and the cell membrane. Tissues vary greatly in size, component and microstructure; they are optically inhomogeneous. Given the larger size and increased hemoglobin content in the liver and the spleen, it is expected that the light signal would be greatly reduced. These differences may also be attributed to the light absorption by other tissue constituents and to light scattering by lipid membranes and cell fragments. When using fluorescence intensity in optically heterogenous samples for quantitative purposes, careful method development and validation should be performed.

In conclusion, although fluorescence imaging confers certain advantages for convenient biodistribution studies, the quantitative data from whole organs is dramatically affected by the scattering and the absorption properties of the organ. The fluorescence intensity detected by fluorescence imaging is not necessarily proportional to the number of molecules present. Fluorescence imaging is very practical and informative in initial experiments to demonstrate the whole-body distribution, unfortunately it yields only qualitative and semi-quantitative images due to artifacts from tissue heterogeneities. To study

the biodistribution of macromolecules quantitatively, methods such as radiotracing or mass spectrometry should be considered. Thus, in **Chapter 4** and **Chapter 5**, the PK and biodistribution of LCP NPs were measured using nanoparticles containing ^{3}H labeled oligonucleotide.

CHAPTER 3

CHARACTERIZATION OF LCP NP FORMULATION

In the present study, the LCP NP formulation (size around 30 nm) was used for two reasons. First, its unique core-membrane structure allows us to readily modify the surface with different lipids and various amounts of PEGylation (**Figure 3.1**). Second, LCP NPs can be easily purified due to the density difference between the particle and the extra excipient, which permits accurate surface characterizations (**Figure 3.2**). In this chapter, we demonstrate that LCP NPs were structured around a lipid bilayer-core and had a size of approximately 30nm. Fluorescence quantification estimated that up to 20% (molar percent of outer leaflet lipids) PEG could be grafted on the surface of LCP NPs. The presence of PEG on the surface of NPs can be characterized using X-ray photoelectron spectroscopy (XPS); a substantial increase in the C-O peak in high resolution C1s scans is an indication of PEG, the intensity of the increase is directly proportional to the PEG concentration on the surface. SANS measurements indicated that at the concentration of 20% at 40 °C, the surface PEG existed in a collapsed and entangled manner, instead of adopting the widely speculated, well-extended brush conformation.

3.1   INTRODUCTION

To date, the characterization of NPs in terms of PEG density is only studied casually with many reports simply using an assumption of complete insertion of the input PEG molecules. To measure the PEG concentration on the surface of NPs accurately, it is necessary remove the unincorporated PEG molecules by filtration or centrifugation based on the difference in size or density. The LCP nanoparticles prepared by the method described in **2.2** contain extra lipids (e.g. DOTAP or DOPC, Cholesterol and DSPE–PEG$_{2000}$). To determine the accurate concentration of DSPE–PEG$_{2000}$ on the surface of LCP NPs, sucrose gradient centrifugation was used to separate LCP NPs with extra lipids. Sucrose gradient centrifugation is commonly used in cell biology to separate the cellular organelles or macromolecules based on their density. The technique involves density gradients prepared by altering the sucrose concentration such that the top of the tube contains liquids of the lowest density and the bottom contains those with the greatest. In the presence of centrifugal force, dispersed particles migrate through the gradient until they reach a zone of density that is equal to their own. LCP NPs containing a calcium phosphate core are heavier than particles that only consist of lipids. Sucrose gradients were prepared by superimposing equal volumes of sucrose solutions layer by layer at decreasing concentrations. The LCP NPs containing dense CaP cores banded tightly at a certain position of sucrose solution, while the unassociated lipid was present as a smear at the top, as shown in **Figure 3.2**.

While many of the PEG molecules are associated with the particles, they are not necessarily presented on the surface. Thus, the fluorescent labeling may overestimate the loading level, especially when large excesses of PEG are used in the preparation process. The

difference in zeta-potential of the NPs with and without PEG is an indication that PEG has coated the surface. We also performed XPS high-resolution carbon 1s scans. XPS is a very powerful surface analytical tool which allows characteristic elemental detection, chemical state identification, and quantification. XPS survey scans are known to be very effective in characterizing the PEG chains that have been grafted onto various solid matrices such as silicon and polystyrene. High resolution C1s scans provide more in-depth information from the characteristic C-O peak, with its intensity directly proportional to the PEG concentration on the surface.

To investigate the conformation of PEG on surfaces of LCP NPs, we employed SANS in situ in water. SANS has emerged as a powerful, noninvasive technique used to characterize the structures of materials on solid and liquid surfaces and interfaces. Importantly, due to their low energies, cold neutrons do not bring any damage on sometimes fragile polymeric samples. SANS is also a bulk probe giving rise to the average polymer conformation over the entire sample. The water fraction inside the polymer layer can also be estimated. Detailed information of SANS is provided in **APPENDIX A**.
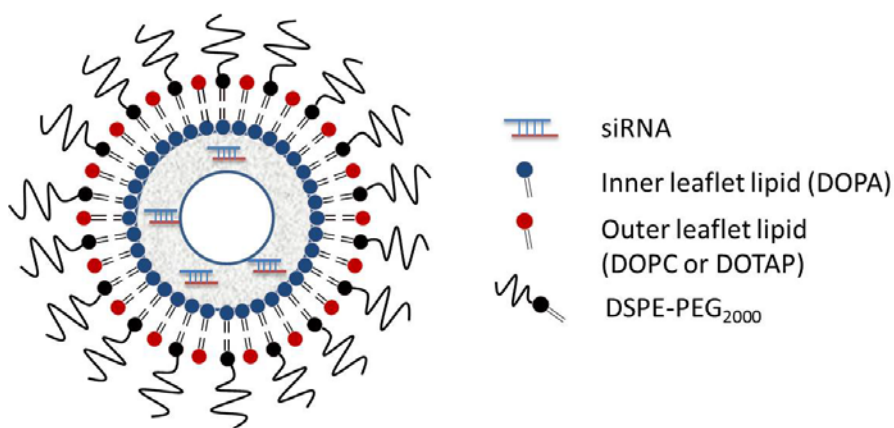
Figure 3.1 Proposed lipid bilayer-core structure of LCP NPs.
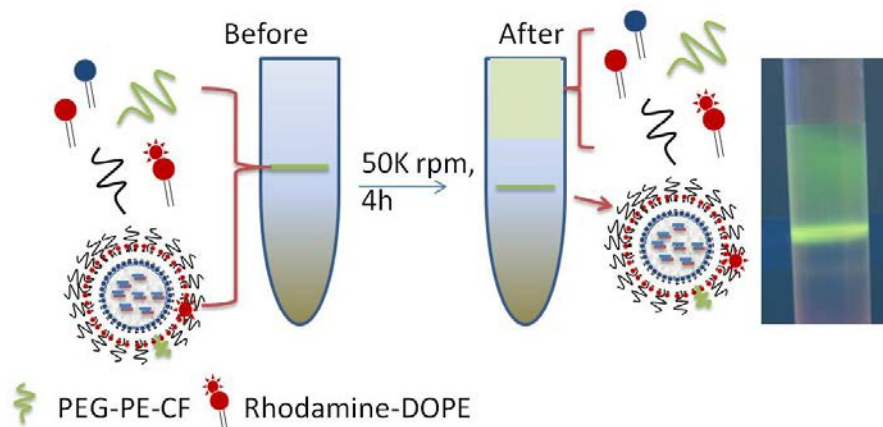
Figure 3.2 Schematic illustration of sucrose gradient centrifugation for purification.

3.2   MATERIALS AND METHODS

3.2.1   Materials

22-mer oligonucleotides (sense sequence, 5'-CAAGGGACTGGAAGGCTGGG-3',) labeled with Texas Red or Cy5.5 Dye (excitation/emission wavelengths of 550/600 nm and 650/700nm, respectively), were purchased from Sigma, Inc. Both Texas Red and ^{3}H-labeled oligonucleotides were used to mimic siRNA. Dioleoylphosphatidylcholine (DOPC), dioleoylphosphatydic acid (DOPA), 1,2-distearoyl-sn-glycero-3-phosphoethanolamine-N-[poly(ethylene glycol)2000] (DSPE-PEG$_{2000}$), Rhodamine-dioleoyl-phosphatidylethanolamine (Rhodamine-DOPE) and 1,2-distearoyl-*sn*-glycero-3-phosphoethanolamine-N-[poly(ethylene glycol)2000-N'-carboxyfluorescein] (DSPE-PEG-CF) were purchased from Avanti Polar Lipids, Inc. (Alabaster, AL).

41

3.2.2 Experimental animals

All work performed on animals was in accordance with and approved by the University of North Carolina Institutional Animal Care and Use Committee. Pharmacokinetics and biodistribution studies of LCP NPs were performed in normal athymic nude (nu/nu) mice and mice carrying H460 human lung cancer xenografts. Tumors were allowed to grow to a size of around 0.2cm^3 before injections.

3.2.3 NP preparations

NPs were prepared using the method described in **Chapter 2**. Two mg/mL Texas Red or ^{3}H-labeled oligonucleotides in 8 mL cyclohexane oil phase (71% cyclohexane with 29% Igepal CO-520 as surfactant), and 2) 100 μL of 100 mM pH 9.0 Na_2HPO_4 also in 8 mL cyclohexane oil phase plus 320 μL of 20 mM DOPA as the inner leaflet lipid. After mixing the above two solutions for 45 min, 30 mL of absolute ethanol was added to the micro-emulsion and the mixture was centrifuged at 12,500 g for 15 min to precipitate the CaP core. After being washed with ethanol 2–3 times, the pellets were dispersed in 500 μL chloroform and stored in a glass vial for further modification. The outer leaflet lipid coating was created by mixing 200 μL of 20 mM cholesterol, 200 μL of 20 mM DOPC, and 100 μL of 20 mM of DSPE-PEG$_{2000}$ with the core. After removal of the chloroform, the core was first suspended in a small volume of ethanol and then dispersed in 5 % Dextrose.

3.2.4 Sucrose gradient centrifugation

The discontinuous sucrose gradient was created with 0.9 mL each of 60% sucrose, 40% sucrose, 20% sucrose and deionized water layered consecutively from bottom to top in 4 ml ultracentrifuge tubes. The mixture containing LCP NPs and extra lipids was applied between 10% sucrose and water. The gradients were centrifuged using a Beckman Coulter SW 60Ti rotor at 168,000g for 4 h at 20°C and then separated into aliquots removed from top to bottom. The fractions were then diluted with ethanol and lysis buffer (0.1% Triton-100 and HCl, pH=2.5) for further measurements. For the SANS experiment, LCP NPs were purified using ^2H_2O and ^2H-sucrose.

3.2.5 Transmission electron microscopy

The size and morphology of the condensed CaP core were determined by transmission electron microscope (TEM) with an acceleration voltage of 100 kV. To prepare the samples, CaP core suspended in CHCl3 (2 µL) were deposited onto a 200 mesh copper grid coated with carbon (Ted Pella, Inc., Redding, CA), followed by air drying at room temperature. Images were acquired using a JEOL 100CX II TEM.

3.2.6 Dynamic light scattering and Zeta potential

The final products, LCP NPs with different lipids grafted to their surface, were diluted with water appropriately. Zeta potential and particle size of the LCP NPs were determined by using a Malvern ZetaSizer Nano series (Westborough, MA).

3.2.7 Fluorescence-labeled lipids analysis

To identify the composition of each faction, Rhodamine-DOPE, DSPE-PEG$_{2000}$-CF and ^{3}H labeled oligonucleotide were used to label the outer leaflet lipid, PEG$_{2000}$-DSPE and CaP core, respectively. The LCP NPs were prepared and purified as described above. The fractions were analyzed using a fluorescence spectrometer and liquid scintillation counter.

3.2.8 X-ray photoelectron spectroscopy study

LCP NPs with varying PEG surface concentrations were prepared and purified as described above and the sucrose was removed. Concentrated LCP NPs were then placed onto a gold substrate, forming a thin, uniform layer. The samples were degassed under vacuum before introduction to the XPS stage. A Kratos Axis Ultra DLD X-ray Photoelectron Spectrometer (Kratos Analytical Ltd.) was used to make the XPS measurements, analyzing the elemental composition of the top 5nm of the sample surface. High-resolution scans of the carbon 1s photoelectron were used to obtain the intensity of the C-O carbon peak, which is

characteristic of a PEG chain. All scans of carbon 1s photoelectrons were peak-fitted using software provided with the instrument.

3.2.9   Small angle neutron scattering study

SANS data were collected on the EQ-SANS instrument of the Spallation Neutron Source of Oak Ridge National Laboratory [106]. A sample-to-detector distance of 4m was employed.   The instrument was operated in the 30 Hz, frame-skipping mode using a minimum wavelength (λ) of 2.5 Å to produce two bands of neutrons (2.5 Å $< \lambda_1 <$ 6.1 Å and 9.4 Å $< \lambda_2 <$ 13.4 Å). This method provides an effective q-range of 0.005 Å^{-1} to 0.42 Å^{-1}, 2 and θ is the scattering angle. The sample temperature was controlled by a water bath. Data

reduction, which was completed using the MANTID software package (http://www.mantidproject.org/), followed standard procedures to correct for incident neutron flux, detector sensitivity, wavelength-dependent transmission, dark current (electronic noise and cosmic radiation) and solvent scattering. The reduced data were azimuthally averaged into $I(q)$ vs. q. The instrument resolution at a given q-value in the final, reduced data was determined to be the weighted average of the instrument resolutions for the wavelengths contributing to that particular q-bin. The data from the two different wavelength bands were merged into a single profile using the method implemented in MANTID. A polydispersed core-with-3-shell spherical model developed at the National Institute of Standards and Technology (NIST) Center for Neutron Research (NCNR) using IGOR Pro software was used to fit the SANS data [64, 107].

3.2.10 Statistical analysis

All statistical analyses were performed by a two-tailed student t-test. Data were considered statistically significant when P value was less than 0.05.

3.3   RESULTS

3.3.1   Size, morphology and surface charge of LCP NPs

Characteristics of purified LCP NPs are summarized in **Table 3.1**. All the NPs were PEGylated at an optimal density of 20% molar ratio of the total outer leaflet lipid. Both LCP-DOTAP and LCP-DOPC NPs had a hydrodynamic diameter of about 30 nm. When the particles were formulated with DOPC as the outer leaflet lipid, the zeta potential was approximately -10 mV. In contrast, when DOTAP was employed, the surface potential became around 15 mV. The slightly positive surface charge might be an indication of PEG modification on the NPs, in contrast to that of pure DOTAP liposomes (~70 mV). At a concentration as high as 20%, the PEG coating is supposed to achieve steric shielding of the NPs' surface and thus create the "stealth" property [46, 61].

The images of the CaP cores were taken without staining, allowing the observation of the size of the cores, which was approximately 10 – 15 nm. The TEM images indicated that the outer layers of the particles also had high electron intensity, but the inner layers had a lower intensity, suggesting that the CaP cores were of a hollow structure (**Figure 3.3**).

Table 3.1 A summary of characteristics of LCP NPs.

Lipid	PEG $_{2000}$		
	Size (nm)	Zeta potential (mV)	Optimal PEG Conc. (molar % of outer leaflet lipids)
DOTAP	~30	15	~ 20
DOPC	~30	-10	~ 20
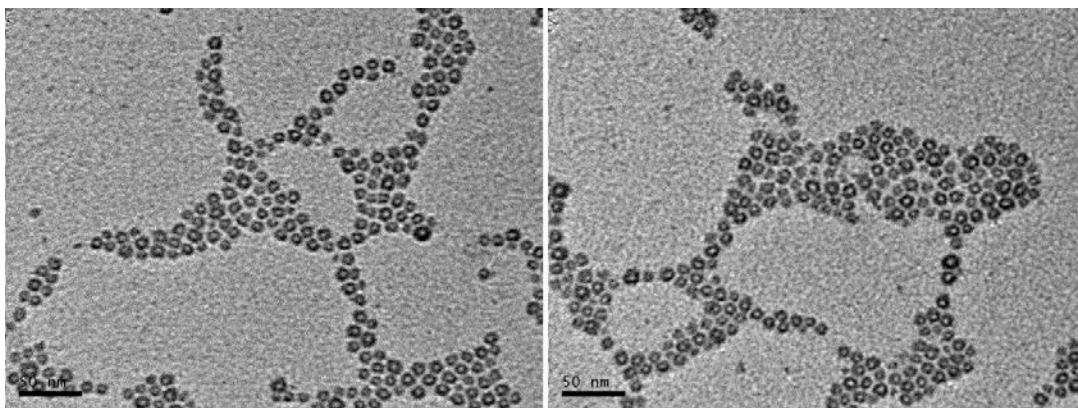
Figure 3.3 TEM image of CaP cores.

Scale bar indicates 10 μm.

3.3.2   Surface coverage of PEG

As discussed above, the LCP NPs prepared using the method described in **2.2** contain extra lipids. To determine the accurate concentration of DSPE–PEG$_{2000}$ on the surface of LCP nanoparticles, sucrose gradient centrifugation was used to separate LCP NPs from the extra lipids. The LCP NPs containing dense CaP cores banded tightly at the interface

between the layer of 20% and 40% sucrose, while the unassociated lipids were present as a smear from the top of the gradient to the interface between 20% and water (**Figure 3.2**). We found that the isolated purified LCP NPs contain around 90% tritium and calcium (by inductively coupled plasma mass spectrometry, ICP-MS). Rhodamine-DOPE, DSPE-PEG$_{2000}$-CF and trace amounts of tritium were detected in the fractions of lower sucrose concentrations, suggesting that extra lipids could be separated from the dense nanoparticles using this method.

Rhodamine-DOPE and DSPE-PEG$_{2000}$-CF were used to measure the molar ratio of DSPE-PEG$_{2000}$-CF in the total outer leaflet lipid. Quantification of DSPE-PEG-CF on purified LCP NPs is summarized in **Figure 3.4**. The addition of a PEG solution during the preparation process produced nanoparticles with approximately the same concentration of PEG as the addition. For example, using 10% PEG-phospholipid solution resulted in purified NPs with 10% PEG-phospholipid. A saturation of PEG incorporation was observed at 20% molar ratio of the total outer leaflet lipid. Furthermore, the charge of the substrate lipid did not influence the amount of PEG coating. No significant difference was found between LCP NPs coated with positively charged lipid DOTAP and neutral lipid DOPC.
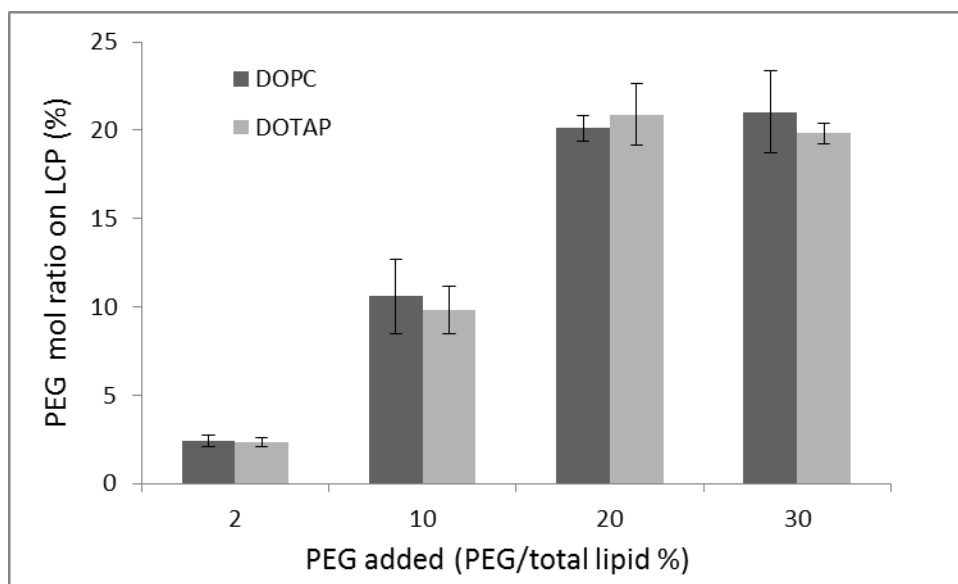
Figure 3.2 Quantitative analysis of DSPE-PEG-CF on purified LCP NPs.

XPS high-resolution carbon 1s scans were used to determine the presence of the PEG on the surface. LCP NPs without PEGylation (0% PEG) were used as a control. **Figure 3.5** shows the high-resolution carbon 1s scan for surface of LCP NPs with 20%, 10% and 0%. The peaks were resolved into various components, corresponding to C-C and C-H bonds at 285.0 eV, C-O bond at 286.5 eV, and to C=O bond at higher energy level. The presence of PEG on the nanoparticle surface can be characterized by a substantial increase in the C-O peak in high resolution C1s scans with its intensity directly proportional to the PEG concentration on the surface, thus enabling the quantitative determination of PEG on the surface [108]. The scans clearly show the growing intensity of the C-O peak at 286.5 eV as the PEG concentration increases, indicating the increasing grafting density of PEG. It is difficult to calculate the exact amount of the PEG due to the presence of C-O in the lipid

layer. However, most of the C-O signal comes from the PEG coating and the trend of these observations confirms the presence of the PEGylation on the surface of LCP NPs.
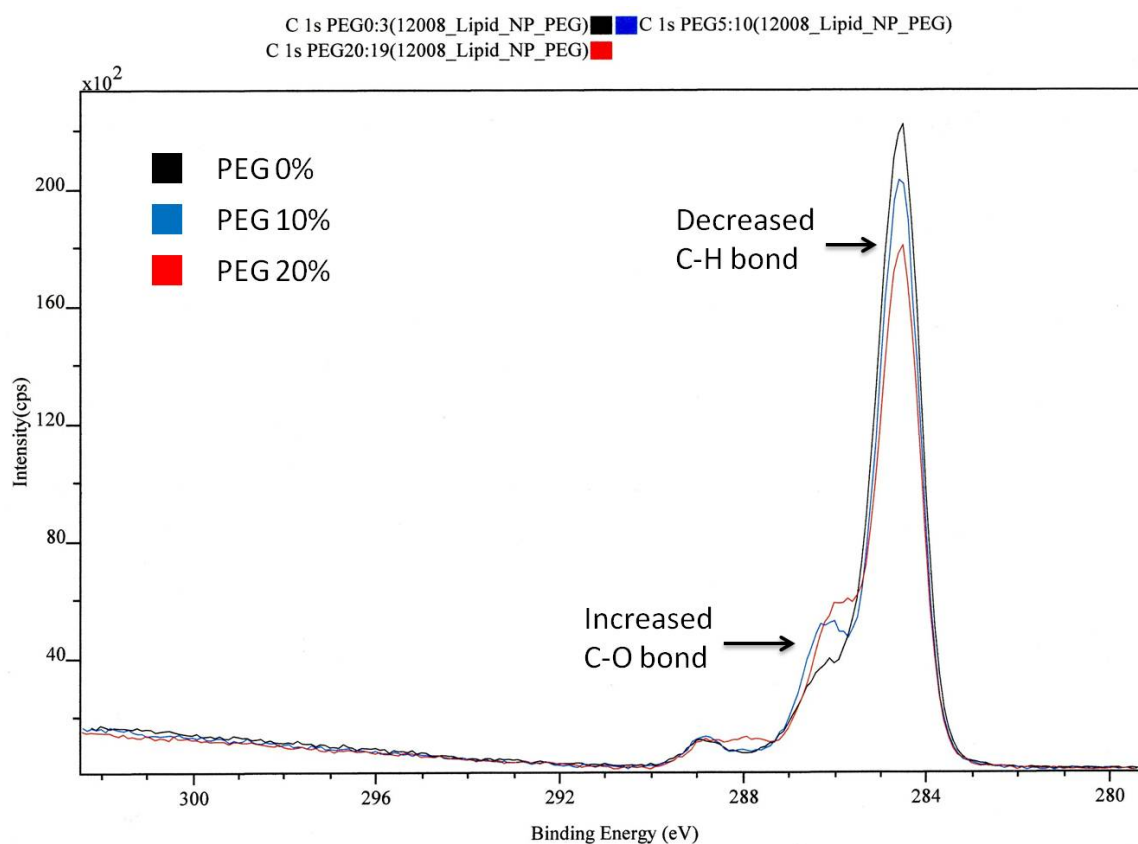
Figure 3.3 High resolution carbon 1s scans of LCP NPs with different amount of PEGylation.

Scale bar indicates 10 μm.

3.3.3 Conformation of surface-grafted PEG

SANS measurements on the samples at different temperatures (10 and 40 ^{o}C) were conducted in order to investigate the PEG conformation on the surface of LCP NPs. It has

50

been reported that the elevation of temperature leads to a decrease in solubility of PEG in water, resulting in a transition of polymers with PEG side chains in an extended state into PEG chains with a collapsed state [109]. Therefore, the SANS curves of the LCP NPs are expected to differ at different temperatures, as shown in **Figure 3.6**. The varying size distribution of LCP particle size (judged by TEM micrograph in **Figure 3.3**) creates difficultly when fitting the whole q range. Therefore, we focused on the largest difference between the SANS data occurring at 10 and 40 ^{o}C (q > 0.02 Å-1). Presumably the difference results from the temperature response of the PEGylated lipids on the surface of the LCP. The intensity within a q range of 0.23 and 0.5 Å-1 increases when the sample is at 10 ^{o}C due to the extension of PEG chains on the LCP surface.

Based on the TEM images (**Figure 3.3**), LCP has a hollow core (possibly water) and a shell (possibly CaP). From the scheme of microemulsion, a bilayer with DSPE-PEG at the outer leaflet should be expected. However, this bilayer was not observed in TEM, perhaps due to a low contrast. Following these observations, the polydispersed core-with-3-shell spherical model is used to fit the SANS data. The three shells represent the CaP, lipid and hydrated PEG regions, moving from the inside to the outside, respectively. Since the amount of sucrose and the concentration of LCP cannot be precisely determined during the sample preparation, obtaining absolute scattering intensity of the system provides no advantages. In order to minimize the number of variables and avoid a local minimum, most of the fitting parameters are constrained according to the physical properties or information from the TEM results. The initial values and the allowed varying range with respect to scattering length densities (SLDs) of the solvent (solv), the hydrated PEG layer (PEG), the lipid bilayer (lip) and CaP (CaP) and hollow core (core) were set to be $(6 \times 10^{-6} \pm 10\%)$, $(3 \times 10^{-6} \pm 100\%)$, $4 \times 10^{-}$

[7] (fixed), ($3.9 \times 10^{-6} \pm 10\%$) and ($6 \times 10^{-6} \pm 10\%$) Å^{-2}, respectively. The average radius of the hollow core, Rcore and thickness of CaP, tCaP were initially set to be 35 and 30 Å, respectively, based on the TEM data, while the lipid bilayer thickness (tlip) was constrained in the normal range between 20 and 40 Å. The final, best-fitting parameters of the model for the 10 $^{\circ}$C data were solv = 5.5×10^{-6} Å^{-2}, PEG = 1.85×10^{-6} Å^{-2}, lip = 4×10^{-7} Å^{-2}, CaP = 4.5×10^{-6} Å^{-2}, core = 6.3×10^{-6} Å^{-2}, tcore = 35.7 Å, tCaP = 31.1 Å, tlip = 25 Å and thickness of hydrated PEG (tPEG) = 8.3 Å.

The same parameters were used to fit the 40 $^{\circ}$C data, except for the values of PEG and tPEG, which were allowed to vary freely. As a result, both models agree with the data reasonably well (**Figure 3.6**). The two facts that the hydrated PEG layer decreased from 8.3 Å to nearly 3.7 Å and that the bilayer becomes slightly thicker (from 25 Å to 21 Å) with an increase in temperature are consistent with the collapsed state of PEG chains. Based on the scattering length densities (SLDs) of the hydrated PEG layer and solvent at 10 $^{\circ}$C, the volume fraction of water in the PEG layer is estimated to be ~20%. Since the molecular weight (MW) of PEG is ~2000 g/mol, the radius of gyration (RG) is estimated to be 18 Å [110], resulting in an overlapping concentration ($\sim \frac{M_W}{4\pi R_G^3/3}$) of 0.174 g/mL, which is less than

¼ of the volume fraction of PEG obtained from the SANS data. These results suggest that the PEG layer should exist in a heavily overlapping regime (**Table 3.2**). It should be noted that the best-fit result seems to underestimate the thickness of the hydrated PEG layer on the LCP surface. The discrepancy is possibly attributed to the fact that the model assumes a constant SLD to describe the PEG layer, although, realistically, it may have a diffuse density profile.
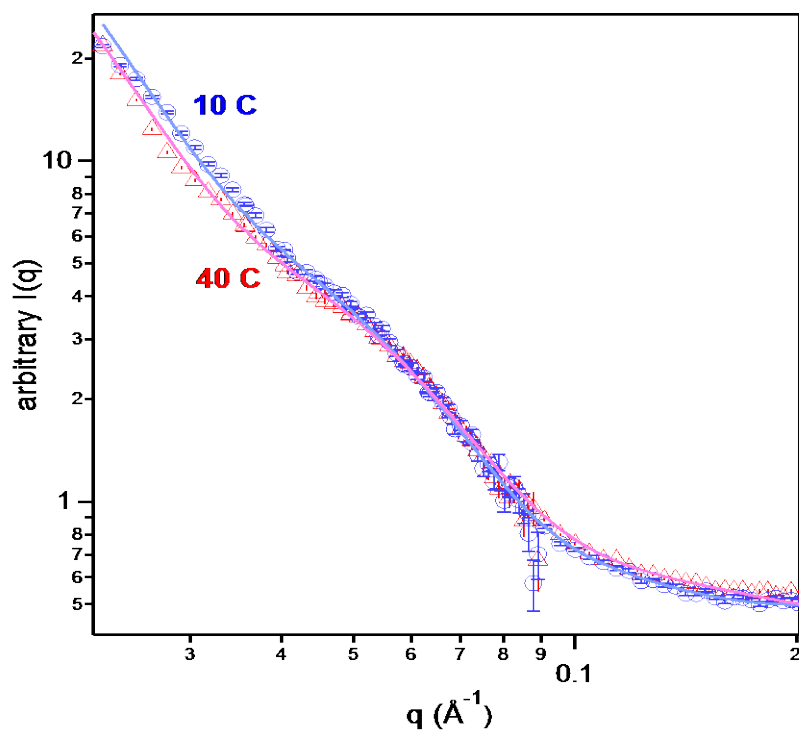
Figure 3.6 SANS data of the LCP NPs at 10 ^{o}C (circles) and 40 ^{o}C (triangles).

The solid lines are best fits to both data sets.

Table 3.2 The thickness of the lipid and PEG layers based on a polydispersed core-with-3-shell spherical model.

	PEG $_{2000}$			
Temp. (°C)	t_{lip} (Å)	t_{PEG} (Å)	water (%)	PEG Conc. (g/mL)
10	25	8.3	20	~ 0.7
40	21	3.7	10	~ 1.4

3.4   DISCUSSION

In this chapter, we demonstrated the ability to formulate a core-membrane structured nanoparticle with full coverage of PEG on the surface. On the basis of fluorescence-labeled PEG analysis, XPS carbon 1s scans, and SANS modeling, a densely grafted, inter- and intra-molecular entangled PEG layer was observed.

Our group [79], and others in the early 1990s [111], demonstrated RES avoidance and long circulation half-life achieved by surface incorporation of PEG in liposomes. This method employs PEG-phospholipids which could by anchored on the lipid membrane by hydrophobic interactions. Due to the amphiphilic nature of the PEG-phospholipids, the degree of surface PEGylation is quite limited; usually less than 5 % if the lipid membrane integrity is to be preserved [61]. However, high density of PEG is necessary to achieve steric shielding of the nanoparticles' surface and thus create the "stealth" property. The unique core-membrane structure of LCP NPs presents an efficient and robust platform for high density PEGylation. In this formulation, the inner leaflet lipid (DOPA) is known to strongly interact with cations (Ca) in the core and is therefore supported and stabilized by the solid and positively charged core. Owing to this substrate-membrane interaction, the supported bilayer has greater stability than unsupported liposomal bilayers [112, 113] and permits a high amount of incorporated DSPE-PEG$_{2000}$, a detergent-like surfactant. This platform provides an opportunity to modify the formulation with a high-density PEG coating and explore the impact of a PEG coating on the *in vivo* behavior of nanoparticle formulation.

By labeling DSPE-PEG$_{2000}$ with a green fluorescent dye, it was determined that LCP nanoparticles could tolerate as much as 20% PEG-phospholipids. XPS analysis verified that

the surface of LCP NPs was covered by a substantial amount of PEG. SANS further estimated that these PEG chains should exist in a heavily overlapping regime, forming a collapsed and entangled polymer layer on the surface. In all cases, there was good agreement between the measurements obtained from each method. Although it is widely accepted that, theoretically, a very high grafting density usually translates to a PEG brush, our findings suggest that a compact polymer layer is present. To the best of our knowledge, there are no reports on direct evidence regarding lipid-based NP surfaces modified with a PEG-based brush. Due to the large excluded volume and large number of hydrogen bonds of PEG chains, the energy penalty of the polymer chains adopting an extended conformation would be extremely high. Therefore, a surface in which PEG chains exist as a tangled mass is energetically favored.

CHAPTER 4

PHARMACOKINETICS AND BIODISTRIBUTION OF LCP NP

We have developed an LCP NP formulation with a well-defined lipid bilayer-core structure to examine the effect of PEG density and different surface lipids on the *in vivo* fate of NPs. It has been demonstrated that 20% (molar percent of outer leaflet lipids) could be grafted on the surface of LCP NPs. The surface PEG existed in a collapsed and entangled manner. The PK and biodistribution studies of LCP NPs formulated with DOPC and DOTAP as the surface lipids were conducted in normal and tumor-bearing mice. The densely PEGylated LCP displayed a biphasic clearance profile. NPs were taken up by the liver, spleen and tumor after their intravenous injection. A substantial amount of the injected dose was observed in the liver. Within the liver, confocal microscopy revealed that LCP NPs were localized in hepatocytes; Kupffer cell uptake was absent. Uptake of LCP by Kupffer cells and splenic macrophages appeared when the surface PEG density decreased to below 15%. LCP NPs with DOTAP exhibited higher accumulation in the liver than LCP NPs with DOPC.

4.1   INTRODUCTION

To be useful *in vivo*, NPs must avoid opsonization and subsequent recognition by macrophages. This can be accomplished through PEGylation [114]. Surface-modification of NPs with PEG has been widely used to prolong the circulation time and improve *in vivo* performance of various nanoscaled carriers. The success of PEGylation critically depends on the steric stabilization conferred by PEG chains on the surface of the NPs. Stabilization is achieved through the highly hydrophilic and flexible nature of PEG chains, which provide repulsive interactions with biological components *in vivo.* The ways in which grafted PEG forms a well hydrated barrier layer on the surface, sterically hindering protein adsorption, were thoroughly discussed in **Chapter 1**.

We have demonstrated that the LCP NP formulation can effectively deliver siRNA [99, 103] to both solid and metastatic tumors. In **Chapter 3**, we showed that the surface of NPs containing a supported lipid bilayer could be modified with a high amount of PEG (20 mol%). A complete shielding of the NP surface was found with a neutral or slightly positive zeta potential. The data suggest that the NPs with full surface protection may show improved EPR effect, improving solid tumor delivery.

Here, we investigated the *in vivo* PK and biodistribution of the LCP NPs in normal and tumor bearing mice. This formulation was chosen for two reasons; first, the unique membrane-core structure allows for modification of the surface with various amounts of PEGylation. Second, LCP NPs can be purified based on the density difference between the particle and the extra excipient, which permits accurate surface characterizations of PEGylation. We have studied the physical conformation of the PEG chains at high graft

density and correlated with the PK and tissue distribution of the modified LCP NPs after intravenous administration. The results of the experiment have revealed some surprising conclusions that are not predicted by existing theories. We believe these findings will benefit the rational design and application of PEG and other hydrophilic polymers for the development of effective drug carrier systems.

4.2   MATERIALS AND METHODS

4.2.1   Materials

22-mer oligonucleotides (sense sequence, 5'-CAAGGGACTGGAAGGCTGGG-3',) labeled with Texas Red or Cy5.5 Dye (excitation/emission wavelengths of 550/600 nm and 650/700nm, respectively), were purchased from Sigma, Inc. Both Texas Red and ^{3}H-labeled oligonucleotides were used to mimic siRNA. Dioleoylphosphatidylcholine (DOPC), dioleoylphosphatydic acid (DOPA), 1,2-distearoyl-sn-glycero-3-phosphoethanolamine-N-[poly(ethylene glycol)2000] (DSPE-PEG$_{2000}$) were purchased from Avanti Polar Lipids, Inc. (Alabaster, AL). NCI-H460 human lung cancer cells were obtained from American Type Culture Collection.

4.2.2   Experimental animals

All work performed on animals was in accordance with and approved by the University of North Carolina Institutional Animal Care and Use Committee.

Pharmacokinetics and biodistribution studies of LCP NPs were performed in normal athymic nude (nu/nu) mice and mice carrying H460 human lung cancer xenografts.

4.2.3 NPs preparation

LCP NPs were prepared as previously described in the **Chapter 2**. The formulations were used without further purification.

4.2.4 PK study

PK studies of LCP NPs were performed in normal nude mice and mice carrying H460 human lung cancer xenografts. Tumors were allowed to grow to a size of around 0.2 cm^3 before injections. Animals were intravenously injected with in LCP NPs containing ^3H labeled oligonucleotide at a dose of 0.25 mg/kg. At selected time points, mice were sacrificed and blood was collected through parallel sampling. The amount of ^3H labeled oligonucleotide in the blood was quantified using liquid scintillation counting. Under the assumption that the total blood volume in the mouse is 7% of its body weight, NP concentrations in the blood were calculated.

4.2.5 Tissue distribution study

Tissue distribution studies of LCP NPs were performed in normal athymic nude mice and mice carrying H460 human lung cancer xenografts. Tumors were allowed to grow to a size of around 0.2 cm^3 before injections. Animals were intravenously injected with LCP NPs

containing ^{3}H labeled oligonucleotide at a dose of 0.25 mg/kg. At selected time points, mice were sacrificed and the heart, liver, spleen, lungs, kidneys and tumors were collected. The tissues were dissolved in NCS Tissue Solubilizer (GE Healthcare, Life Sciences) and the amount of ^{3}H labeled oligonucleotide in the different tissues was quantified using liquid scintillation counting.

4.2.6 Cell-type specific localization by confocal microscopy

Mice were intravenously injected with Texas Red-labeled oligonucleotides contained in different LCP NP formulation four hours before sacrifice and tissue collection. Tissue blocks were immediately frozen in OCT (Tissue-Tek, Dublin, OH) on dry ice, allowing the generation of ten-µm-thick cryosections. The tissue sections were then mounted on Superfrost Plus slides (Fisher Scientific Co., Houston, TX). After a brief rinsing with PBS to remove any surface embedding medium, we completed fixation of the particles with acetone at -20 °C. Then, tissue sections were stained with Alexa Fluor 488 phalloidin (Life Technologies) and mounted in a medium containing DAPI (Vector Lab.). Images were captured using an Olympus FV1000 MPE confocal microscope under three channels: DAPI for nuclei, Alexa Fluor 488 for phalloidin, and Texas Red for oligonucleotide.

4.2.7 Statistical analysis

Data are presented as the mean ± SD.

4.3   RESULTS

4.3.1   Blood Clearance

The blood clearance kinetics 4 h after injection are shown in **Figure 4.1**. No significant differences in the PK profiles were observed between the tumor free and the tumor-bearing mice treated with LCP NPs containing ^{3}H-labeled oligonucleotide. NPs in both types of mice showed a rapid distribution phase, in which serum concentrations dropped dramatically within the first 30 min. After that, concentrations remained steady for at least 3.5 h. A standard bi-exponential clearance model was used to describe the blood concentrations of NPs using WinNonlin Version 5.2 (Pharsight, St. Louis, MO). Between fifty and sixty percent of the injected dose (ID) was cleared with a half-life of around 15 min in the distribution phase; the rest was cleared with a longer half-life of 6 h in the clearance phase.
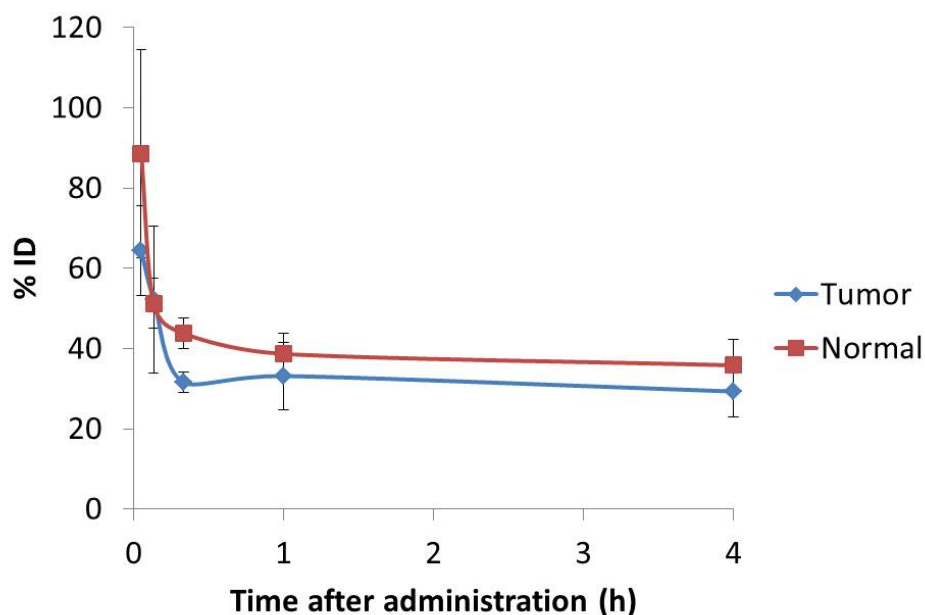
Figure 4.1. Pharmacokinetics of LCP NPs in normal and tumor-bearing mice.

Data are plotted as % injected dose vs time (N=4). The outer leaflet lipid is DOPC. PEG concentration is 20% (molar percent of outer leaflet lipids).

4.3.2 Kinetics of tissue distribution

To investigate the kinetics of the LCP NPs' distribution into major organs, we performed the biodistribution study during the 4 h after injection. The tumor-free and tumor-bearing mice demonstrate nearly identical distribution kinetics in major organs (**Figure 4.2A and B**). A rapid increase in the ^{3}H signal in the liver and spleen (usually considered to be RES organs) coincided with the initial distribution phase in the plasma. The ^{3}H signal reaches a plateau about 1 h after injection. This lack of accumulation may indicate that NPs extravasate from liver sinusoids into the space of Disse, but are not taken up to a significant degree by resident macrophages or hepatocytes. At 4 h after injection, the liver and spleen

showed significant accumulation of the ^{3}H signal (~25% ID and 15% ID, respectively), both in excess of that in the tumor (<5% ID). No significant signal accumulated in the kidney, indicating that the particles do not disintegrate or release the encapsulated cargo in circulation. Despite complete NP PEGylation, substantial amount of accumulation still occurred in the RES organs (liver and spleen). A fairly small percentage of the dose reaches the tumor site. The results also show that blood clearance and tissue distribution kinetics are approximately equal in both tumor-free and tumor-bearing mice.
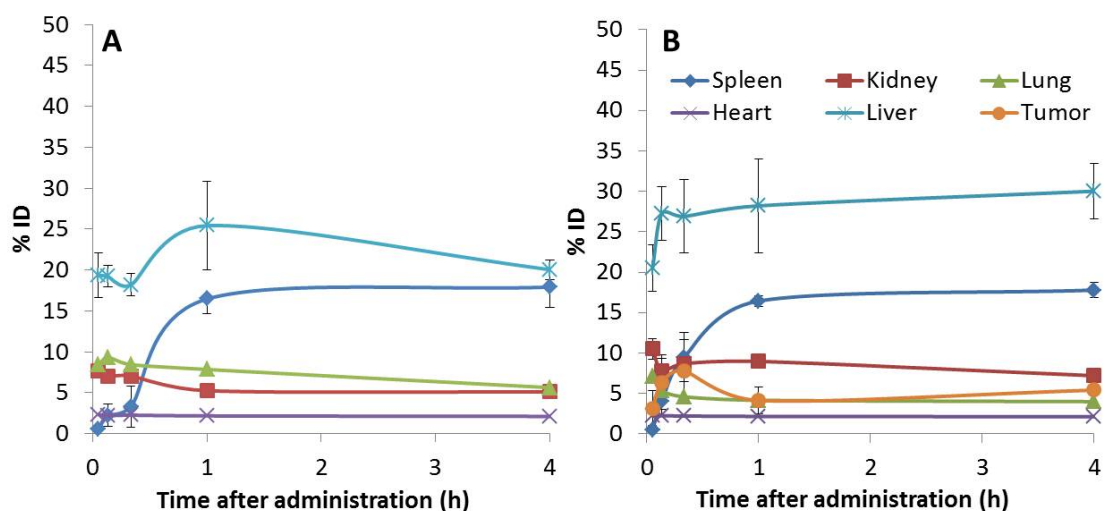
Figure 4.2 Tissue distribution of LCP NPs as a function of time after administration.

(A: normal mice; B: tumor-bearing mice. N=4) Data are plotted as % injected dose vs time. The outer leaflet lipid is DOPC. PEG concentration is 20% (molar percent of outer leaflet lipids).

4.3.3 Cell-type specific localization in liver and spleen

PEG dependence of hepatocytes delivery was investigated using LCP NPs with various amounts of PEG coating. Confocal microscopy of liver sections harvested from mice

4 h after injection of nanoparticles containing Texas Red-labeled oligonucleotide are shown in Figure 6. Tissues were stained with phalloidin to visualize cell membranes of all cell types. Significantly, preferential accumulation of the Texas Red-labeled oligonucleotide in hepatocytes (also called liver parenchymal cells, which contain large DAPI-stained blue nuclei) was observed in mice treated with LCP NPs containing a high density of PEG (**Figure 4.3A5-6**). Distribution was generally homogenous throughout the different zones and the liver acinus. Hepatocyte uptake was markedly reduced by decreasing the amount of PEG on the surface of nanoparticles. LCP NPs with a lower density of or completely without PEG rarely entered hepatocytes (**Figure 4.3A2 and 3**). Instead, they experienced phagocytic uptake by Kupffer cells and resided in hepatic sinusoids (a region between hepatocytes as indicated by the arrow, **Figure 4.3**). Inspection of the spleen revealed that substantial Texas Red signals were found localized in the red pulp region in mice treated with LCP NPs containing a lower density of PEG. A very limited amount of signal in the spleen was observed in tissues injected with LCP NPs coated with a high PEG density (**Figure 4.3B**). This observation is consistent with the significant uptake of low and high-PEG LCP NPs by Kupffer cells and hepatocytes, respectively, in the liver. These results are evidence that delivery to the hepatocytes is enabled by grafting a dense PEG layer on the surface of LCP NPs. They also suggest that PEG concentration determines cell-type specific localization at the tissue level. We conclude that LCP NPs with a high PEG density (~20%) completely evaded RES and accumulated primarily in the hepatocytes.
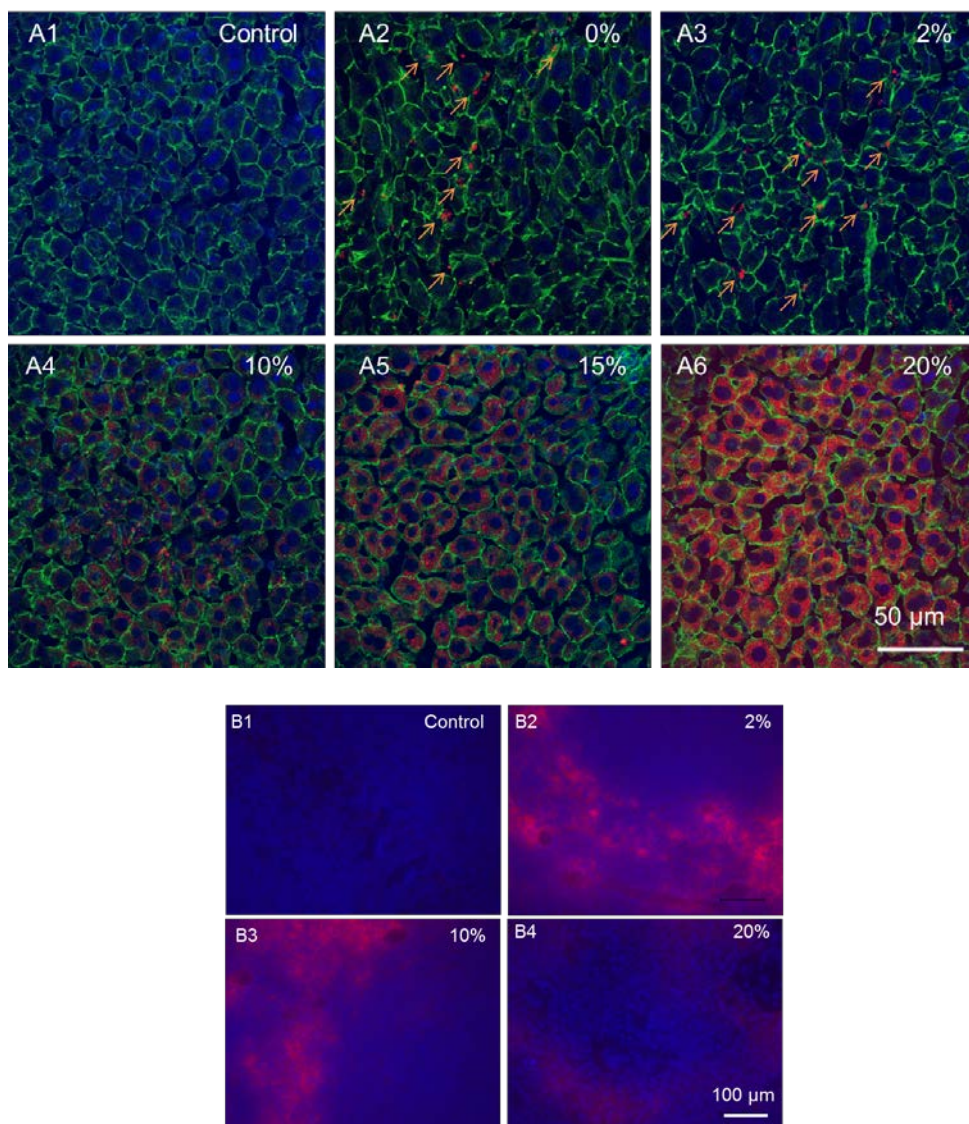
Figure 4.3 Cell-type specific localization of LCP NPs in liver (A) and Spleen (B).

DAPI for nuclei, Alexa 488 for phalloidin, and Texas Red for oligonucleotides. Percentages indicate amount of PEG-DSPE2000 incorporated in the outer leaflet of the wrapping lipid bilayer of LCP NPs. Arrows indicate representative Kupffer cell uptake.

4.4   DISCUSSION

Despite complete nanoparticle PEGylation, significant accumulation still occurred in the RES organs (liver and spleen); only a minor amount of the dose accumulated in the tumor. The results also show that blood clearance and tissue distribution kinetics are approximately equal in both tumor-free and tumor-bearing mice. This is likely a consequence of the small size of the LCP nanoparticles (~30nm). Extravasation in the liver is plausible because the presence of fenestrae in liver sinusoids, which measure 100 nm in diameter in mice [14]. This condition can be described by a two-compartment model with, as shown in **Figure 4.4**. Nanoparticle elimination from the central compartment occurred due to RES uptake and distribution to the peripheral compartment (tissues with discontinuous endotheliums), where X_b, X_T and X_L are the amount of NPs in blood, tumor and liver, respectively. K_{10} is the elimination rate constant from the central compartment by RES uptake and $K_{12, 21, 13, 31}$ are the intercompartmental transfer rate constants. V_T and V_L are the volume of distribution of tumor and liver, respectively. For simplicity, we are assuming that these processes are all occur in a first-order fashion. The tumor tissue retains NPs due to a lack of lymphatic drainage; consequently, K_{21} would be negligible compared with other intercompartmental transfer. K_{10} depends on the properties of the NPs, such as size and surface chemistry, which was discussed in **Chapter 1**.

In this study, PEG density and the EPR effect are the determinants of K_{10} and K_{12}, respectively. The PK and biodistribution results suggest that the distribution of small, long-circulating NPs to tissues with discontinuous endotheliums could become competing kinetic processes (i.e. K_{12} and K_{13}), dependent on the properties of nanoparticles, vasculature

permeability, and blood flow. Given the limited blood flow through the tumor and its relatively small volume, a highly perfused organ with a discontinuous endothelium, such as the liver, can easily outpace the tumor and thus become the major distribution site.

The significant uptake by the hepatocytes is of great interest to formulation design in biomedical applications due to its importance in many infectious and metabolic disorders. On the other hand, it highlights a potentially important complication in the development of nanoparticles regarding imaging and therapeutic applications in oncology. Recently, there is increasing evidence that small nanoparticles in the size range of 10-30 nm can more effectively penetrate the physiological barriers imposed by tumor vasculature and the interstitial matrix than larger particles [88, 115]. Similarly, avoiding rapid distribution to the liver will be another critical design criterion for future nanoparticle systems targeting tumor sites.
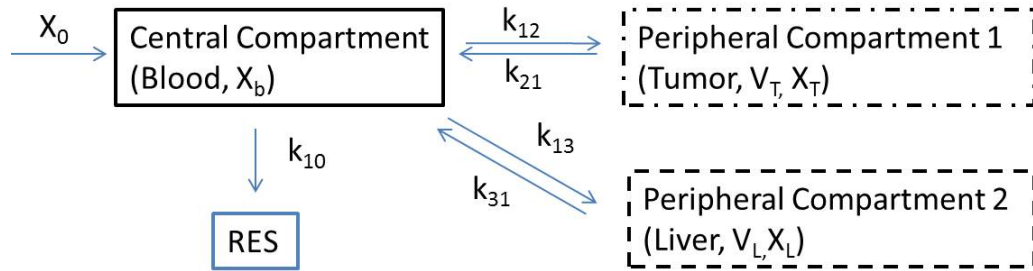
Figure 4.4 Proposed two-compartment PK model in the tumor-bearing mice.

X_0 = injected dose; X_b X_T X_L=concentration in blood, tumor and liver;
V =volume of distribution, k_{10}= clearance coefficient;
$K_{12, 21, 13, 31}$=transportation coefficient.

In summary, we have shown that a high density of PEG coating with heavily overlapped and collapsed regime was placed on the surface of LCP NPs. This PEG coating enables delivery to the hepatocytes and avoidance of RES uptake, although whether the hepatocyte uptake is specific to lipid-based nanoparticles is still unknown. This study established a relationship between the physicochemical properties of nanoparticles and their *in vivo* pharmacokinetics and biodistribution profile, which may provide important information for a rational formulation development approach.

CHAPTER 5

PROTEIN ADSORPTION AND ITS IMPACT ON IN VIVO BEHAVIOR

PK and biodistribution of nanoparticulate carriers are controlled by a complex array of interrelated physicochemical and biological factors. Surface chemistry of NPs has been identified as one of the key determinants of these characteristics. LCP NPs are an effective drug delivery system to both solid and metastatic tumors. The well-defined lipid bilayer-core structure of the LCP NPs allows us to examine the effect of different surface lipids on the *in vivo* fate of NPs. The PK and biodistribution studies of LCP NPs formulated with DOPC and DOTAP were conducted in normal and tumor-bearing mice. NPs were taken up by the liver, spleen and tumor after their intravenous injection. LCP NPs with DOTAP exhibited higher accumulation in the liver than LCP NPs with DOPC. Analysis of NP-bound proteins revealed that apoE might serve as an endogenous targeting ligand for LCP-DOTAP NPs, but not LCP-DOTAP NPs. The enhanced liver accumulation with LCP-DOTAP NPs was reduced in apoE deficient mice. In all, characteristics of the surface lipids played important roles in influencing PK and biodistribution of LCP NPs. Understanding the NPs-protein interaction is necessary for rational engineering of NPs with favorable *in vivo* behavior.

5.1 INTRODUCTION

In comparison to bulk biomaterials, NPs have an extremely high surface-to-volume ratio. Control of their surface properties is crucial to their *in vivo* performance. The surfaces of NPs are immediately covered by proteins after they have been injected into the blood. The absorption of proteins to such surfaces confers a new "biological identity" to NPs in the biological milieu, which is what cells, tissues and organs actually "see" when interacting with NPs [67]. This new "bio-nano interface," created by covering NPs with a complex layer of protein "corona" determines the subsequent cellular/tissue responses and biological consequence [68, 69]. Surface characteristics such as charge, hydrophilicity and curvature dictate the extent and specificity of protein binding [67, 70]. Specific protein binding is one of the key elements that affect biodistribution of the NPs. Indeed, a detailed knowledge of NP-protein interaction is vital for the rational formulation design and optimization of nanoparticles.

The aim of the present study was to identify the influence of surface lipid composition on the PK and biodistribution of LCP NPs. Moreover, we investigated the underlying mechanism in terms of the nature of the adsorbed proteins. The unique bilayer-core structure of LCP NP formulation allows for readily modification of the surface with different lipid. Thus, this single tool may serve as a platform for the rational design and investigation of novel lipid-based drug carriers. The *in vivo* biodistribution and pharmacokinetics studies of LCP NPs modified with DOPC and DOTAP were conducted in normal and tumor-bearing mice. We then analyzed the composition of the protein corona which bound the NPs with difference surface chemistry, using one-dimensional sodium

dodecyl sulfate polyacrylamide gel electrophoresis (SDS-PAGE) and matrix-assisted, laser-desorption ionization, time-of-flight mass spectrometry (MALDI-TOF-MS). The results suggested that the enrichment of apolipoproteins on the surface of LCP-DOTAP NPs might be the explanation of its enhanced liver accumulation. This information is helpful in determining the advantages and disadvantages of the outcome for the various proteins and facilitating development of effective drug carriers.

5.2   MATERIALS AND METHODS

5.2.1   Materials

22-mer oligonucleotides (sense sequence, 5'-CAAGGGACTGGAAGGCTGGG-3',) labeled with Texas Red or Cy5.5 Dye (excitation/emission wavelengths of 550/600 nm and 650/700nm, respectively), were purchased from Sigma, Inc. Both Texas Red and ^{3}H-labeled oligonucleotides were used to mimic siRNA. Dioleoylphosphatidylcholine (DOPC), dioleoylphosphatydic acid (DOPA), 1,2-distearoyl-sn-glycero-3-phosphoethanolamine-N-[poly(ethylene glycol)2000] (DSPE-PEG$_{2000}$) were purchased from Avanti Polar Lipids, Inc. (Alabaster, AL). NCI-H460 human lung cancer cells were obtained from American Type Culture Collection.

5.2.2   Experimental animals

All work performed on animals was in accordance with and approved by the University of North Carolina Institutional Animal Care and Use Committee. Pharmacokinetics and biodistribution studies of LCP NPs were performed in normal athymic nude (nu/nu) mice and mice carrying H460 human lung cancer xenografts. ApoE-deficient mice (ApoE-/-, stock #002052) and wild type C57BL/6 mice were obtained from Jackson Laboratories (Bar Harbor, ME).

5.2.3   NPs preparation

NPs were prepared as previously described in **Chapter 2**. The particles were purified using sucrose gradient centrifugation as described in the **Chapter 2** to enable the completion of a protein adsorption assay. The formulation was used without further purification in all of the animal studies.

5.2.4   PK study

PK study of LCP-DOTAP was performed in normal mice and mice carrying H460 human lung cancer xenografts. Tumors were allowed to grow to a size of around 0.2 cm^3 before injections. Animals were intravenously injected with in LCP NPs containing ^{3}H labeled oligonucleotide at a dose of 0.25 mg/kg. At given time intervals, four animals were

sacrificed for blood collection. Radioactivity was measured using liquid scintillation counting.

5.2.5 Tissue distribution

Biodistribution studies of LCP NPs were performed in normal athymic nude (nu/nu) mice and mice carrying H460 human lung cancer xenografts. Tumors were allowed to grow to a size of around $0.2cm^3$ before injections. Animals were intravenously injected with in LCP NPs containing ^3H labeled oligonucleotide at a dose of 0.25 mg/kg. Four hours after injection, animals were sacrificed for tissue collection. The tissue samples were processed as described in **Chapter 4**. Radioactivity was measured using liquid scintillation counting.

5.2.6 Cell-type specific localization in liver

Confocal microscopy imaging of the frozen section of liver was conducted as described in **Chapter 4**.

5.2.7 Determination of the protein corona composition

LCP NPs with different surface lipids and PEG densities were prepared and purified as described above. Samples were incubated at different serum concentrations (20% and 80%). NPs were allowed to incubate with the serum solutions for 1.5 hours. After the incubation, the samples were centrifuged to pellet the particle-protein complexes, separating them from the supernatant. Afterwards, the pellets were washed three times with PBS and

then re-suspended in PBS in a protein loading buffer. Gel electrophoresis was performed at 120V, 400mA for about 60 minutes. The gels were stained in coomassie blue staining and destained overnight in 50% methanol, 10% acetic acid [116, 117].

After the separation of proteins by SDS-PAGE, bands were excised from the gel and digested with trypsin, and the resulting peptide mixtures were separated and analyzed by MALDI-TOF-MS (ABI 4800 MALDI TOF/TOF). Spectra were analyzed by MASCOT software to identify tryptic peptide sequences matched to the NCBI database (http://www.ncbi.nlm.nih.gov/).

5.2.8 *In vivo* apoE dependency

LCP NPs containing ^{3}H labeled oligonucleotide were administered intravenously via the tail vein at a dose of 0.25 mg/kg into ApoE-deficient mice and wild type C57BL/6 mice, respectively. Four hours after injections, major organs were collected from animals and processed for radioactivity measurements.

5.2.9 Statistical analysis

Data are presented as the mean $\pm$ SD. The statistical significance was determined by using the student's t-test. P values of <0.05 were considered significant.

5.3   RESULTS

5.3.1   Blood Clearance

As shown in **Figure 5.1**, no significant differences in the pharmacokinetic profiles were observed between the tumor free and the tumor-bearing mice treated with LCP NPs containing ^{3}H-labeled oligonucleotide. The clearance of LCP NPs from the bloodstream was bi-exponential. NPs in both types of mice showed a rapid distribution phase, in which serum concentrations dropped to around 50% ID within the first 30 min. The rapid distribution is not surprising considering that the small size of the particle and accumulation of the nanoparticles was mainly caused by passive entrapment through the discontinuous endothelium of the liver. The 20% PEG coating in the formulation is stable in the biological environment (data not shown here) and would be sufficient to effectively block the adsorption of opsonic proteins at the early time of period after injection. The substrate lipid could influence the rate of clearance in the β phase. LCP-DOPC NPs possessed a longer half-life at the β phase than their DOTAP counterparts.
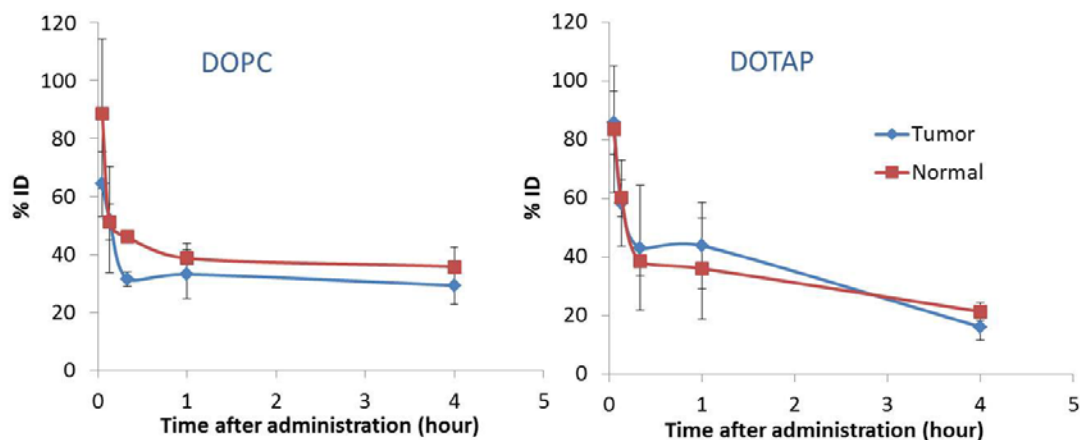
Figure 5.1. Pharmacokinetics of LCP NPs with different lipid in normal and tumor-bearing mice.

Data are plotted as % injected dose vs time (N=4). PEG concentration is 20% (molar percent of outer leaflet lipids).
The data of LCP-DOPC NPs is Figure 4.1. The data was placed here for easy comparison with that of LCP-DOTAP NPs.

5.3.2 Tissue distribution

Figure 5.2 shows the tissue distribution of LCP NPs at 4 h post-injection. The particles were distributed mainly in the liver, spleen and tumor. This observation is consistent with the fact that these tissues are lined with discontinuous or leaky endothelium that allows for passive entrapment of foreign particulates [118]. Despite the accumulation in the tumor, biodistribution profiles of the LCP NPs in tumor bearing mice were not significantly different from their normal controls. The substrate lipid didn't change the global tissue distribution pattern significantly. It is interesting to note that, however, the accumulation level of NPs was greatly enhanced in the liver by DOTAP compared with that of DOPC

76

(60% ID versus 30% ID). It is likely that the faster clearance of LCP-DOTAP NPs in the β

phase is due to this enhanced uptake by liver.
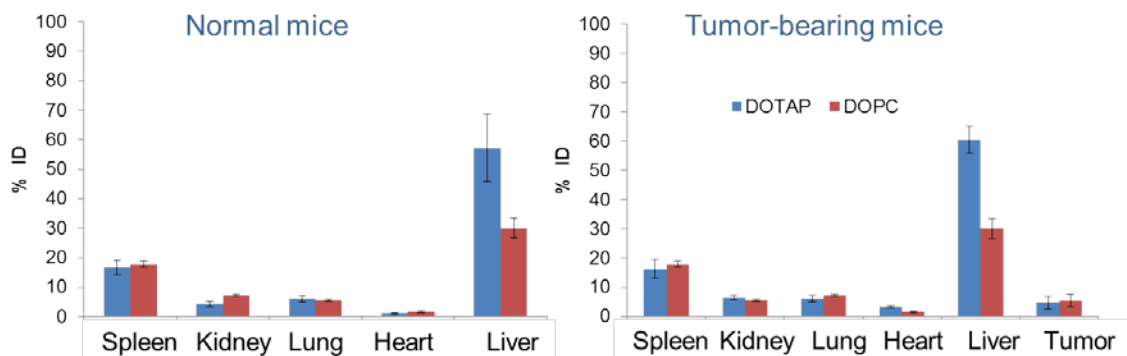
Figure 5.2 Tissue distribution of LCP NPs with different lipid.

(A: normal mice; B: tumor-bearing mice. N=4) Data are plotted as % injected dose vs time.
The outer leaflet lipid is DOPC. PEG concentration is 20% (molar percent of outer leaflet
lipids).

5.3.3   Cell-type specific distribution

To obtain direct evidence whether LCP NPs entered hepatocytes or were sequestered

by kupffer cells *in vivo*, we injected mice with LCP NPs containing Texas Red-labeled

oligonucleotide and observed the tissue sections under confocal microscopy. Cell-type

specific distribution and the lipid dependence of hepatic delivery were investigated. Confocal

microscopy of liver sections taken from mice 4 h after the injection of NPs are shown in

Figure 5.3. Tissue sections were stained with Alexa488-phalloidin (green) to visualize cell

membranes of hepatocytes and with DAPI (blue) for all nuclei. Preferential accumulation of

the Texas Red-labeled oligonucleotide in hepatocytes was observed in mice injected with

77

LCP-DOTAP NPs. Only minor amounts of signal were associated with nonparenchymal cells in the liver sinusoids (**Figure 5.3B and C**). Distribution was generally homogenous throughout the different zones and the liver lobules. Replacement of DOTAP on the NPs with DOPC resulted in markedly reduced hepatocyte uptake (**Figure 5.3C**).
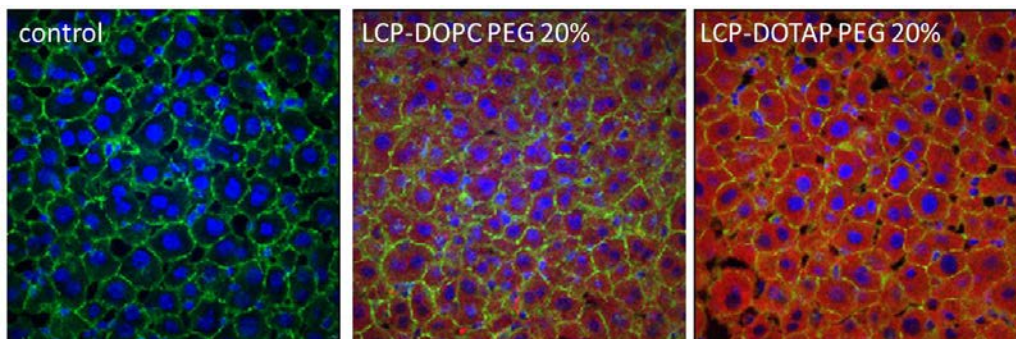
Figure 5.3 Cell-type specific localization of LCP NPs with different lipid in liver.

DAPI for nuclei, Alexa 488 for phalloidin, and Texas Red for oligonucleotides. DOPC and DOTAP were in the outer leaflet of the wrapping lipid bilayer of LCP NPs, respectively.

5.3.4   Composition of protein corona

To investigate the mechanisms causing higher uptake of LCP-DOTAP NPs by hepatocytes, LCP-DOTAP and DOPC NPs with different amounts of PEGylation were incubated with serum. The resulting protein corona was analyzed for protein identification. The NP-protein complexes were washed three times to get rid of the proteins with low affinity for the NP surface. NPs were incubated with 20% or 80% serum. The higher protein: nanoparticle ratio may be more representative of the true biological conditions in the bloodstream.

SDS-PAGE gel of serum proteins obtained from the LCP NP-protein complexes is shown in **Figure 5.4**. The main spots on the gels were HSA, IgG, and the apolipoproteins. Particles made of DOPC with a different PEG density exhibited similar qualitative compositions of their plasma protein adsorption patterns. This observation was consistent with some literature indicating that despite the net decrease in the amount of proteins bound with PEGylated NPs, protein profiles of the PEGylated NPs were not significantly different than their uncoated controls [117]. For LCP-DOTAP NPs with 5%, specific bands of apolipoproteins apo E and apo A-II (**Figure 5.4**, band 5and 7) were observed. Besides, when increasing the PEG content in the NPs to 20 %, a decrease in Complement C3 adsorption was achieved. We hypothesize that LCP NPs with 20% PEG could gradually shed off PEG coating after administration, due to the sink conditions provided by the serum proteins, exposing the substrate lipid. Once attached to the surface of hepatocytes, LCP-DOTAP NPs with apo E can enter the cells via receptor-mediated endocytosis. In contrast, LCP-DOPC NPs were merely transiently associated with the liver and were re-distributed out of this organ without significant internalization.
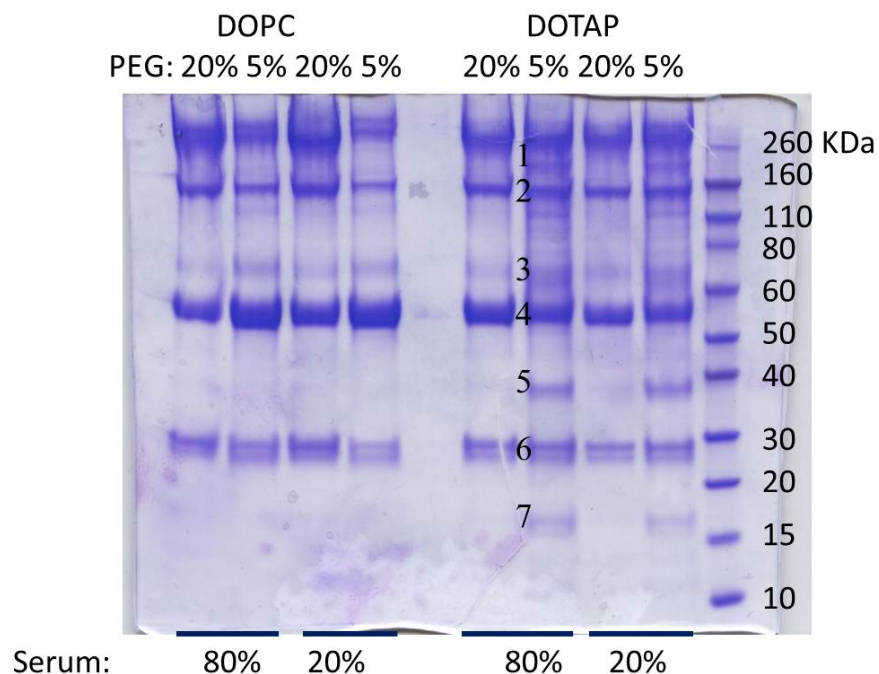
Figure 5.4 SDS-PAGE gel of serum proteins obtained from LCP NP-protein complexes following incubation at different serum concentrations.

The molecular weights of the proteins in the standard ladder are reported on the right for reference. The numbers reported close to the gel bands for LCP-DOTAP NPs with 5% PEG in 80% serum indicate that those bands were cut out and analyzed with MS.

Table 5.1 Representative proteins associated with LCP-DOTAP NPs with 5% PEG incubated in 80% serum, as identified by LC MS/MS.

Band number	Gel band Mw (kDa)	Protein identity
1	190	Complement C3
2	150	IgG Apolipoprotein B
3	65	Serotransferrin Clusterin
4	55	HSA
5	38	Apolipoprotein E
6	28	Apolipoprotein A-I (HDL)
7	16	Apolipoprotein A-II (HDL)

5.3.5 *in vivo* apoE dependency

To determine whether apoE is indeed responsible for the specific delivery of LCP NPs to hepatocytes, biodistribution studies were performed in wild-type and apoE−/− mice. The biodistribution in apoE−/− mice demonstrated identical levels in hepatic accumulation between LCP-DOTAP and LCP-DOPC NPs (**Figure. 5.5**). In contrast, in wide type mice, LCP-DOTAP NPs mediated an enhanced accumulation of the dose in the liver. No significant difference was found in the detected signals in other major organs. These results validated the findings of our protein adsorption studies and suggested that the targeting of LCP-DOTAP NPs to hepatocytes may be apo E-denpendent.
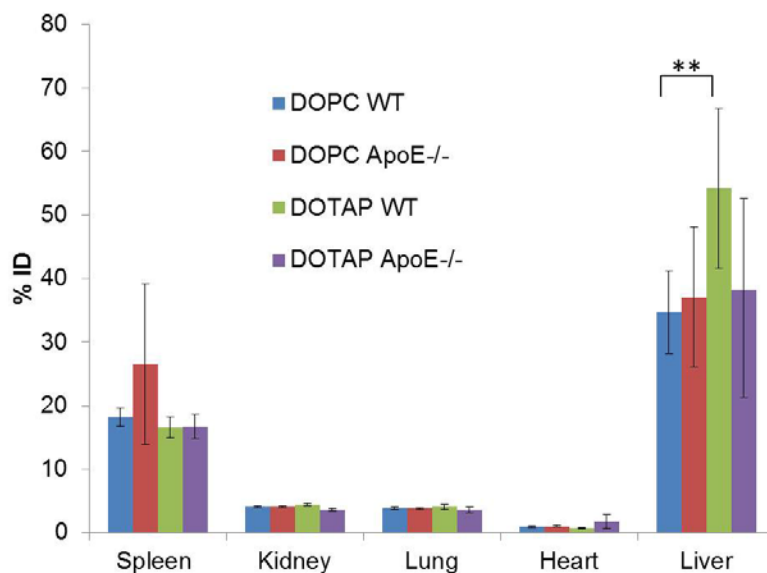
Figure 5.5 Tissue distribution of LCP NPs in wild-type and apoE−/− mice (N=4).

** indicates p<0.05 Formulations: LCP-DOPC and LCP-DOTAP NPs with 20% PEG.

5.4   DISCUSSION

The results presented in this chapter suggest that apoE acts as an endogenous targeting ligand and plays a major role in the β-phase of plasma clearance and hepatic uptake of LCP NPs. LCP-DOTAP NPs were taken up by hepatocytes more than LCP-DOPC NPs. Protein adsorption studies demonstrated that apoE adsorption occurred specifically in LCP-DOTAP NPs. These findings were corroborated by *in vivo* studies in wild-type and apoE−/− mice. The difference in hepatocyte uptake of LCP-DOTAP and LCP-DOPC NP observed in wild-type mice was almost completely absent in apoE−/− mice. The relatively large variation

of liver uptake in apoE−/− mice might be due to the alterations in gene expression profile and serum lipoprotein composition.

It has been reported that cationic lipid-based NPs may recruit apoE as an endogenous ligand *in vivo*. Multiple receptors have been associated with apoE-mediated uptake, such as low-density lipoprotein receptors (LDLR), many other members of the LDLR, and scavenger receptors, which are also expressed on the surface of hepatocytes. These systems usually contain a total PEG‐lipid in the formulation less than 5 mol% [119]. It is interesting to note that with 20% PEG on the surface, the substrate lipid still plays a critical role in determining the *in vivo* fate of NPs. One possible explanation is that the PEG coating gradually sheds off in circulation and the presence of surface charge may facilitate specific protein-membrane interaction.

About 80% of liver cells are hepatocytes, which constitute the parenchyma of the liver tissues, and the others are non-parenchymal cells, including Kupffer cells, endothelial cells, extrathymic T cells localized in sinusoids, and Ito cells (also called stellate cells) localized in the space of Disse [120]. The blood flow after tail vein injection of LCP NPs circulates from the portal vein to the sinusoids then to the central veins. In mice, the LCP NPs delivered by this method could potentially extravasate to space of Disse via the fenestrae with size of about 150 nm in the liver sinusoidal endothelium [121], where the particles come into direct contact with hepatocytes. If the particles are still densely coated with PEG, they will not be taken up by the hepatocytes and may re-enter circulation. K_{13} and K_{31} are the intercompartmental transfer rate constants between the peripheral compartment (liver) and the central compartment (blood), respectively. As the PEG molecules on the surface diffuse, gradually exposing the surface lipid to the *in vivo* environment, the protein corona starts to

form on the surface of the particles, where apo E begins to have an effect as an endogenous targeting ligand. LCP-DOTAP NPs could be internalized by the hepatocytes through receptors such as LDLR through the process of receptor-mediated endocytosis, whereas LCP-DOPC NPs may only enter the hepatocytes through non-specific interactions. It is likely that LCP-DOPC NPs that are not taken up to a significant degree by hepatocytes may re-enter circulation, resulting in a slow clearance in β-phase. The hypothesized mechanism of hepatocyte uptake of LCP-DOTAP and LCP-DOPC NPs was summarized in **Figure 5.6**.

A key drawback of this method of targeting, however, is that the NPs rely on endogenous apo E. As a result, LCP NPs delivered to target cells in the liver might be variable, potentially contributing to toxicity. Attachment of a targeting ligand such as galactose onto the NPs may facilitate hepatocyte targeting and prevent unexpected side effects. Identification and selection of the best markers to differentiate liver parenchymal and non-parenchymal regions are crucial to the success of delivery of LCP NPs to hepatocytes. A series of hepatocyte markers should be tested to determine their targeting effects.
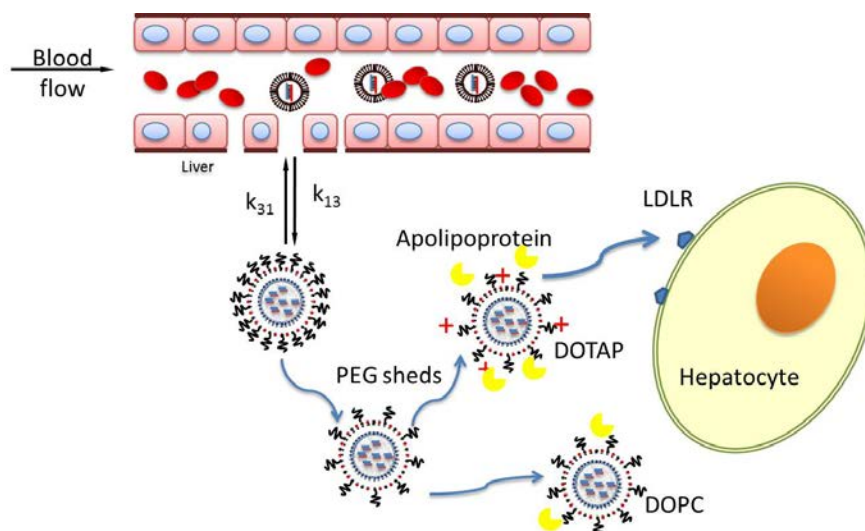
Figure 5.6 Hypothesized mechanism of hepatocytes uptake of LCP-DOTAP and LCP-DOPC NPs.

CHAPTER 6

DISCUSSION

6.1   SUMMARY OF RESEARCH RESULTS AND FUTURE PLANS

It is known that the successful development of nanoparticulate therapeutics relies on the in-depth understanding of their *in vivo* PK and biodistribution, determined by a series of properties of NPs. Here we established a relationship between the physicochemical properties of LCP NPs and their *in vivo* PK and biodistribution profiles, which may provide important information for an approach to rational formulation development. The PK and biodistribution studies were conducted using careful method validation (**Chapter 2**).

With a supported lipid bilayer structure, the LCP NP could accommodate a high degree of PEGylation compared to the conventional liposomes containing a regular lipid bilayer. We have shown that approximately 20 mol% of the outer leaflet of the lipid membrane was modified with DSPE-PEG$_{2000}$, creating an inter- and intramolecular, entangled PEG layer on the surface of the NPs (**Chapter 3**). This densely coated LCP NP showed a biphasic elimination pattern in PK. The rapid clearance in the α-phase was due to extravasation of the NPs to highly fenestrated tissues, such as the liver. Within the liver, LCP NPs delivered cargo to hepatocytes in a PEG concentration-dependent manner, revealed by confocal imaging. A high-density PEG coating enables hepatocyte delivery and avoidance of

RES uptake, although whether the hepatocyte uptake is specific to lipid-based NPs is still unknown (**Chapter 4**).

Additionally, LCP NPs with surface coatings of different lipids exhibit different *in vivo* behaviors after intravenous injections. LCP NPs modified with DOTAP exhibited higher accumulation in the liver than LCP NPs modified with DOPC. These altered pharmacokinetic and biodistribution properties are the product of protein binding patterns of the surface lipids. Analysis of NP-bound proteins revealed that apoE might serve as an endogenous targeting ligand for LCP-DOTAP NPs, but not for LCP-DOPC NPs. The enhanced liver accumulation of LCP-DOTAP NPs was reduced in apoE deficient mice. Thus, *in vitro* characterization obtained after the incubation of the NP-protein complexes might be predictive of the behavior observed *in vivo* (**Chapter 5**).

6.2   FURTHER DIRECTIONS

Our future plan is to 1) further optimize the formulation to enhance the antitumor effect of these particles and 2) utilize the formulation in a suitable liver disease model.

LCP NPs present a convenient platform to incorporate multiple functionalities for cancer therapeutics or imaging. An in-depth understanding of the interactions between NPs and biological systems is of significant interest. Our further studies are aimed at correlating the properties of LCP NPs, such as size, PEGylation and targeting ligands, with blood kinetics, tissue distribution, transportation, and therapeutic or imaging performances. By identifying how size, PEGylation and targeting ligands influence the delivery process, we may then be able to redesign the nanoparticle formulation to maximize accumulation in the tumor (either primary or metastatic). First, we plan to modify the preparation method of LCP NPs to make a series of NPs with different sizes and determine the optimal size for tumor delivery. Second, we plan to employ PEG molecules with different chain lengths. We are going to investigate the effects of low graft densities with high molecular weight PEG *vs.* the higher surface density of low molecular weight polymers on reducing protein adsorption. The conformation of the grafted PEG will also be investigated. Third, we plan to test a series of targeting ligands to enhance to tumor delivery. Recent studies suggested that PEG surface density of NPs had a significant effect on ligand-directed tumor targeting. The highest specificity and targeting efficiency was observed at a low PEG surface density [122]. With well-designed new formulations and further additions of targeting ligand, the performance of LCP NPs on cancer treatment and diagnostics could be improved.

LCP NPs, in particular LCP-DOTAP NPs, exhibited significant accumulation in the liver. NPs delivered in sinusoids or engulfed by Kupffer cells are generally inactive for therapeutic effects and might cause toxicity, However, the hepatocytes are often the cell type of interest for therapeutic application. Many liver diseases, for example, hepatitis B virus infections, hepatocellular carcinoma and liver cirrhosis, pose a serious health challenge worldwide due to the lack of curative treatment options other than liver resection or transplantation.

First, we plan to utilize RNAi therapeutics by using LCP NPs to treat hepatocellular carcinomas. Multiple siRNAs could be encapsulated into a single LCP NP to acheive combination therapy. Second, many antivirus drugs are nucleoside analogues. They can be phosphorylated to form prodrugs and encapsulated into the CaP core of LCP NPs. For long-term clinical application, toxicity would be a primary concern. While the size and surface chemistry are important for their *in vivo* behavior, composition of the NPs is mainly responsible for cytotoxicity. Since calcium phosphate is the principle building component of hard tissues such as bone and tooth enamel, calcium and phosphate ions already exist in the body at millimolar concentrations. The biodegradation products of LCP NPs are thus presumed to be relatively nontoxic. The major concern for the toxicity might be derived from the lipid.

6.3   ENDING REMARKS

Engineered NPs offer an unprecedented opportunity for therapeutic and diagnostic applications. To design the most efficient nanoparticle-based delivery systems, nano-bio interactions must be carefully investigated. Not only will the results facilitate the engineering of NPs, but they will also help our understanding in the morphology and chemistry of nanoscale objects in mediating biological responses. The fundamental studies on nano-bio interactions will enable an approach to the rational formulation development and the nanoengineering process by creating specific design rules. This would also provide a perspective on the construction of complex nanostructures that ensure the highest possible delivery efficiency. *In vitro* characterization of NPs and correlation to their *in vivo* fate could also lead to the development of predictive and simulation tools to assist in the engineering process.

APPENDIX A

Theory of small angel neutron scattering for polymer analysis

A typical neutron diffractometer consists of a source of radiation, a monochromator to select the wavelength, slits to adjust the shape of the beam, a sample and a detector. As shown in **Figure A1**, during a SANS experiment, a beam of neutrons from a reactor is slowed down and properly selected by their speed. The neutrons are then directed at a sample, which can be either an aqueous solution or a solid sample. The neutrons are elastically scattered by nuclear interaction with the nuclei or interaction with magnetic momentum of unpaired electrons. An area detector is used to monitor the diffracted radiation and the position of detector can be adjusted. In zero order dynamical theory of diffraction, the strength of the interaction of a neutron wave with a given nucleus is directly related to the scattering length density (SLD). Different types of system have different natural patterns for the distribution of SLD. In the case of polymer systems, where we have countable repeated units that make up the scattering, we can think about the spatial distribution of those units such that the structure of the polymer might be revealed. The scattering length of nuclei varies randomly across the periodic table and between isotopes of the same element. PEG conformation study utilized the technique of contrast variation (or contrast matching), which takes advantages of the differential scatter of hydrogen and deuterium.
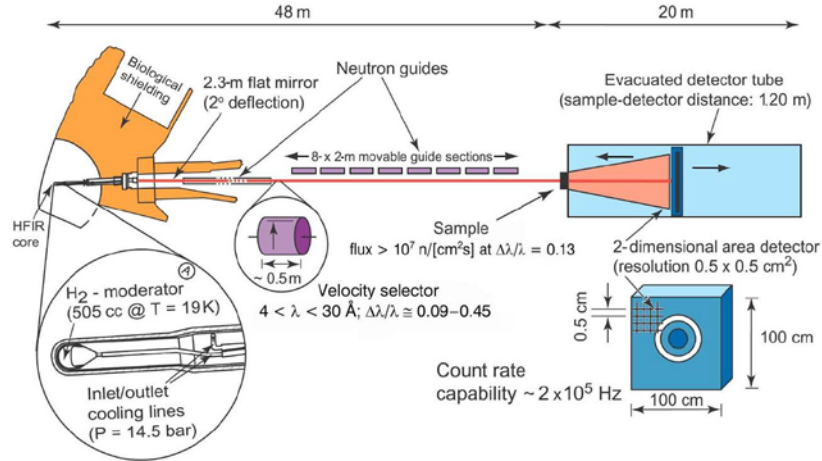
Figure A1. Schematic illustration of general-purpose SANS diffractometer.

(Picture from www. ornl. gov)

In neutron scattering experiments, the momentum transfer (q) for the incident neutron and the scattered neutron were recorded (as shown in **Figure A2**), where $q = k_i - k_s$ with k_i and k_s being the wavevectors of the incoming and scattered neutrons respectively. Scientists measure the intensity of neutrons scattered by matter (per incident neutron) as a function of the variable q. The scattered intensity is often denoted as I (q).
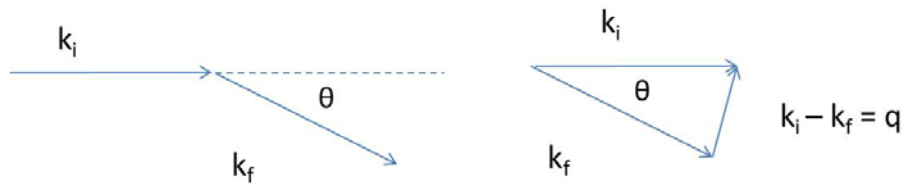
Figure A2. Schematic representation of the momentum initial state and final state during elastic scattering.

There are essentially two classes of data analysis: model-dependent and model-independent. In this study, we used the former method, which consists of building a mathematical model of the SLD distribution to describe the spatial arrangement of the material in the sample.

Yang Liu's publications

Peer-reviewed Papers

- **Liu Y,** Huang L. Influence of lipid composition on pharmacokinetics and biodistribution of LCP Nanoparticles Manuscript in Preparation
- **Liu Y**, Nieh MP, Heller W, Hu Y, Huang L. Nanoparticle delivery to hepatocytes requires a compact, non-brush conformation of the polyethylene glycol coating. In revision
- **Liu Y**, Tseng YC, Huang L. Biodistribution studies of nanoparticles using fluorescent imaging: A qualitative or quantitative method? Pharm Res. 2012 Jul 18.
- **Liu Y**, Huang L, Liu F. Paclitaxel nanocrystals for overcoming multidrug resistance in cancer. Mol Pharm. 2010;7(3):863-9.
- Liu F, Park JY, Zhang Y, Conwell C, **Liu Y**, Bathula SR, Huang L. Targeted cancer therapy with novel high drug-loading nanocrystals. J Pharm Sci. 2010;99(8):3542-51.
- Dong X, Mattingly CA, Tseng MT, Cho MJ, **Liu Y**, Adams VR, Mumper RJ. Doxorubicin and Paclitaxel-loaded Lipid-based Nanoparticles Overcome Multi-Drug Resistance by Inhibiting P-gp and Depleting ATP. Cancer Res. 2009;69(9):3918-26.

Review Papers and Perspectives

- Huang L, **Liu Y**. In vivo delivery of RNAi with lipid-based nanoparticles. Annu Rev Biomed Eng. 2011;13:507-30.
- **Liu Y**, Huang L. Designer lipids advance systemic siRNA delivery. Mol Ther. 2010;18(4):669-70.

Conference Abstracts

- **Yang Liu**, Mu-Ping Nieh, William Heller, Yunxia Hu and Leaf Huang. Nanoparticle delivery to hepatocytes requires a compact, non-brush conformation of the

polyethylene glycol coating. Drug Carriers in Medicine & Biology, Gordon Research Conferences. Waterville Valley, NH, August 2012. Poster Presentation

- **Yang Liu**, Leaf Huang and Feng Liu. Paclitaxel nanocrystals for overcoming multidrug resistance in cancer. Liposome Research Days Conference, Vancouver, Canada, August 2010. Poster Presentation

REFERENCES

1.   Davis, M.E., Z.G. Chen, and D.M. Shin, *Nanoparticle therapeutics: an emerging treatment modality for cancer.* Nat Rev Drug Discov, 2008. **7**(9): p. 771-82.

2.   Reddy, L.H. and P. Couvreur, *Nanotechnology for therapy and imaging of liver diseases.* J Hepatol, 2011. **55**(6): p. 1461-6.

3.   Jain, R.K. and T. Stylianopoulos, *Delivering nanomedicine to solid tumors.* Nat Rev Clin Oncol, 2010. **7**(11): p. 653-64.

4.   Rosen, H. and T. Abribat, *The rise and rise of drug delivery.* Nat Rev Drug Discov, 2005. **4**(5): p. 381-5.

5.   Wagner, V., et al., *The emerging nanomedicine landscape.* Nat Biotechnol, 2006. **24**(10): p. 1211-7.

6.   Wolff, J.A. and D.B. Rozema, *Breaking the bonds: non-viral vectors become chemically dynamic.* Mol Ther, 2008. **16**(1): p. 8-15.

7.   Bragonzi, A., et al., *Biodistribution and transgene expression with nonviral cationic vector/DNA complexes in the lungs.* Gene Ther, 2000. **7**(20): p. 1753-60.

8.   Ishiwata, H., et al., *Characteristics and biodistribution of cationic liposomes and their DNA complexes.* J Control Release, 2000. **69**(1): p. 139-48.

9.   Ishida, O., et al., *Size-dependent extravasation and interstitial localization of polyethyleneglycol liposomes in solid tumor-bearing mice.* Int J Pharm, 1999. **190**(1): p. 49-56.

10.   Whitehead, K.A., R. Langer, and D.G. Anderson, *Knocking down barriers: advances in siRNA delivery.* Nat Rev Drug Discov, 2009. **8**(2): p. 129-38.

11.   Di Guglielmo, G.M., et al., *Distinct endocytic pathways regulate TGF-beta receptor signalling and turnover.* Nat Cell Biol, 2003. **5**(5): p. 410-21.

12.   Fang, C., et al., *In vivo tumor targeting of tumor necrosis factor-alpha-loaded stealth nanoparticles: effect of MePEG molecular weight and particle size.* Eur J Pharm Sci, 2006. **27**(1): p. 27-36.

13.   Alexis, F., et al., *Factors affecting the clearance and biodistribution of polymeric nanoparticles.* Mol Pharm, 2008. **5**(4): p. 505-15.

14.   Braet, F. and E. Wisse, *Structural and functional aspects of liver sinusoidal endothelial cell fenestrae: a review.* Comp Hepatol, 2002. **1**(1): p. 1.

15.   Braet, F., et al., *Contribution of high-resolution correlative imaging techniques in the study of the liver sieve in three-dimensions.* Microsc Res Tech, 2007. **70**(3): p. 230-42.

16.   Matsumura, Y. and H. Maeda, *A new concept for macromolecular therapeutics in cancer chemotherapy: mechanism of tumoritropic accumulation of proteins and the antitumor agent smancs.* Cancer Res, 1986. **46**(12 Pt 1): p. 6387-92.

17.   Hobbs, S.K., et al., *Regulation of transport pathways in tumor vessels: role of tumor type and microenvironment.* Proc Natl Acad Sci U S A, 1998. **95**(8): p. 4607-12.

18.   Jain, R.K., *Delivery of molecular medicine to solid tumors.* Science, 1996. **271**(5252): p. 1079-80.

19.   Olive, K.P., et al., *Inhibition of Hedgehog signaling enhances delivery of chemotherapy in a mouse model of pancreatic cancer.* Science, 2009. **324**(5933): p. 1457-61.

20.   Xiao, K., et al., *The effect of surface charge on in vivo biodistribution of PEG-oligocholic acid based micellar nanoparticles.* Biomaterials, 2011. **32**(13): p. 3435-46.

21.   Schipper, M.L., et al., *Particle size, surface coating, and PEGylation influence the biodistribution of quantum dots in living mice.* Small, 2009. **5**(1): p. 126-34.

22.   Thorek, D.L. and A. Tsourkas, *Size, charge and concentration dependent uptake of iron oxide particles by non-phagocytic cells.* Biomaterials, 2008. **29**(26): p. 3583-90.

23.   Roser, M., D. Fischer, and T. Kissel, *Surface-modified biodegradable albumin nano- and microspheres. II: effect of surface charges on in vitro phagocytosis and biodistribution in rats.* Eur J Pharm Biopharm, 1998. **46**(3): p. 255-63.

24.   Jokerst, J.V., et al., *Nanoparticle PEGylation for imaging and therapy.* Nanomedicine (Lond), 2011. **6**(4): p. 715-28.

25.   Owens, D.E., 3rd and N.A. Peppas, *Opsonization, biodistribution, and pharmacokinetics of polymeric nanoparticles.* Int J Pharm, 2006. **307**(1): p. 93-102.

26.   Moghimi, S.M. and J. Szebeni, *Stealth liposomes and long circulating nanoparticles: critical issues in pharmacokinetics, opsonization and protein-binding properties.* Prog Lipid Res, 2003. **42**(6): p. 463-78.

27. Yamamoto, Y., et al., *Long-circulating poly(ethylene glycol)-poly(D,L-lactide) block copolymer micelles with modulated surface charge.* J Control Release, 2001. **77**(1-2): p. 27-38.

28. Chung, T.H., et al., *The effect of surface charge on the uptake and biological function of mesoporous silica nanoparticles in 3T3-L1 cells and human mesenchymal stem cells.* Biomaterials, 2007. **28**(19): p. 2959-66.

29. Lopes de Menezes, D.E., L.M. Pilarski, and T.M. Allen, *In vitro and in vivo targeting of immunoliposomal doxorubicin to human B-cell lymphoma.* Cancer Res, 1998. **58**(15): p. 3320-30.

30. Zhou, Y., et al., *Impact of single-chain Fv antibody fragment affinity on nanoparticle targeting of epidermal growth factor receptor-expressing tumor cells.* J Mol Biol, 2007. **371**(4): p. 934-47.

31. Farokhzad, O.C., et al., *Nanoparticle-aptamer bioconjugates: a new approach for targeting prostate cancer cells.* Cancer Res, 2004. **64**(21): p. 7668-72.

32. Stella, B., et al., *Design of folic acid-conjugated nanoparticles for drug targeting.* J Pharm Sci, 2000. **89**(11): p. 1452-64.

33. Montet, X., et al., *Multivalent effects of RGD peptides obtained by nanoparticle display.* J Med Chem, 2006. **49**(20): p. 6087-93.

34. Tokatlian, T. and T. Segura, *siRNA applications in nanomedicine.* Wiley Interdiscip Rev Nanomed Nanobiotechnol. **2**(3): p. 305-15.

35. Bartlett, D.W., et al., *Impact of tumor-specific targeting on the biodistribution and efficacy of siRNA nanoparticles measured by multimodality in vivo imaging.* Proc Natl Acad Sci U S A, 2007. **104**(39): p. 15549-54.

36. Kirpotin, D.B., et al., *Antibody targeting of long-circulating lipidic nanoparticles does not increase tumor localization but does increase internalization in animal models.* Cancer Res, 2006. **66**(13): p. 6732-40.

37. Li, S.D. and L. Huang, *Stealth nanoparticles: high density but sheddable PEG is a key for tumor targeting.* J Control Release. **145**(3): p. 178-81.

38. Geng, Y. and D.E. Discher, *Hydrolytic degradation of poly(ethylene oxide)-block-polycaprolactone worm micelles.* J Am Chem Soc, 2005. **127**(37): p. 12780-1.

39. Park, J.H., et al., *Systematic surface engineering of magnetic nanoworms for in vivo tumor targeting.* Small, 2009. **5**(6): p. 694-700.

40. Decuzzi, P., et al., *A theoretical model for the margination of particles within blood vessels.* Ann Biomed Eng, 2005. **33**(2): p. 179-90.

41.   Flory, P.J., *Principles of Polymer Chemistry*. 1971: Cornell Univ. Press, Ithaca, NY.

42.   de Gennes, P., *Conformations of polymers attached to an interface.* Macromolecules, 1980. **13**(5): p. 1069-1075.

43.   Vonarbourg, A., et al., *Parameters influencing the stealthiness of colloidal drug delivery systems.* Biomaterials, 2006. **27**(24): p. 4356-73.

44.   Zolnik, B.S. and N. Sadrieh, *Regulatory perspective on the importance of ADME assessment of nanoscale material containing drugs.* Adv Drug Deliv Rev, 2009. **61**(6): p. 422-7.

45.   Jun, Y.W., et al., *Surfactant-assisted elimination of a high energy facet as a means of controlling the shapes of TiO2 nanocrystals.* J Am Chem Soc, 2003. **125**(51): p. 15981-5.

46.   Marsh, D., R. Bartucci, and L. Sportelli, *Lipid membranes with grafted polymers: physicochemical aspects.* Biochim Biophys Acta, 2003. **1615**(1-2): p. 33-59.

47.   Kenworthy, A.K., et al., *Range and magnitude of the steric pressure between bilayers containing phospholipids with covalently attached poly(ethylene glycol).* Biophys J, 1995. **68**(5): p. 1921-36.

48.   Bedu-Addo, F.K., et al., *Effects of polyethyleneglycol chain length and phospholipid acyl chain composition on the interaction of polyethyleneglycol-phospholipid conjugates with phospholipid: implications in liposomal drug delivery.* Pharm Res, 1996. **13**(5): p. 710-7.

49.   Shimada, K., et al., *Determination of incorporated amounts of poly(ethylene glycol)-derivatized lipids in liposomes for the physicochemical characterization of stealth liposomes.* Int J Pharm, 2000. **203**(1-2): p. 255-63.

50.   Kingshott, P., H. Thissen, and H.J. Griesser, *Effects of cloud-point grafting, chain length, and density of PEG layers on competitive adsorption of ocular proteins.* Biomaterials, 2002. **23**(9): p. 2043-56.

51.   Li, S.D. and L. Huang, *Nanoparticles evading the reticuloendothelial system: role of the supported bilayer.* Biochim Biophys Acta, 2009. **1788**(10): p. 2259-66.

52.   Li, S.D. and L. Huang, *Pharmacokinetics and biodistribution of nanoparticles.* Mol Pharm, 2008. **5**(4): p. 496-504.

53.   Li, S.D., S. Chono, and L. Huang, *Efficient oncogene silencing and metastasis inhibition via systemic delivery of siRNA.* Mol Ther, 2008. **16**(5): p. 942-6.

54.   Zalipsky, S., *Functionalized poly(ethylene glycol) for preparation of biologically relevant conjugates.* Bioconjug Chem, 1995. **6**(2): p. 150-65.

55.   Parrish, B., R.B. Breitenkamp, and T. Emrick, *PEG- and peptide-grafted aliphatic polyesters by click chemistry.* J Am Chem Soc, 2005. **127**(20): p. 7404-10.

56.   Ishida, T., D.L. Iden, and T.M. Allen, *A combinatorial approach to producing sterically stabilized (Stealth) immunoliposomal drugs.* FEBS Lett, 1999. **460**(1): p. 129-33.

57.   Liu, Z., et al., *Circulation and long-term fate of functionalized, biocompatible single-walled carbon nanotubes in mice probed by Raman spectroscopy.* Proc Natl Acad Sci U S A, 2008. **105**(5): p. 1410-5.

58.   Chan, J.M., et al., *PLGA-lecithin-PEG core-shell nanoparticles for controlled drug delivery.* Biomaterials, 2009. **30**(8): p. 1627-34.

59.   Dubertret, B., et al., *In vivo imaging of quantum dots encapsulated in phospholipid micelles.* Science, 2002. **298**(5599): p. 1759-62.

60.   Xia, X., et al., *Quantifying the coverage density of poly(ethylene glycol) chains on the surface of gold nanostructures.* ACS Nano, 2012. **6**(1): p. 512-22.

61.   Garbuzenko, O., Y. Barenholz, and A. Priev, *Effect of grafted PEG on liposome size and on compressibility and packing of lipid bilayer.* Chem Phys Lipids, 2005. **135**(2): p. 117-29.

62.   Levin, C.S., et al., *Determining the conformation of thiolated poly(ethylene glycol) on Au nanoshells by surface-enhanced Raman scattering spectroscopic assay.* Anal Chem, 2006. **78**(10): p. 3277-81.

63.   Garcia-Fuentes, M., et al., *Application of NMR spectroscopy to the characterization of PEG-stabilized lipid nanoparticles.* Langmuir, 2004. **20**(20): p. 8839-45.

64.   Hayter, J.B., *Physics of Amphiphiles--Micelles, Vesicles, and Microemulsions.* 1983.

65.   Engel, M.F., A.J. Visser, and C.P. van Mierlo, *Conformation and orientation of a protein folding intermediate trapped by adsorption.* Proc Natl Acad Sci U S A, 2004. **101**(31): p. 11316-21.

66.   Cedervall, T., et al., *Understanding the nanoparticle-protein corona using methods to quantify exchange rates and affinities of proteins for nanoparticles.* Proc Natl Acad Sci U S A, 2007. **104**(7): p. 2050-5.

67.   Mahmoudi, M., et al., *Protein-nanoparticle interactions: opportunities and challenges.* Chem Rev, 2011. **111**(9): p. 5610-37.

68.   Nel, A.E., et al., *Understanding biophysicochemical interactions at the nano-bio interface.* Nat Mater, 2009. **8**(7): p. 543-57.

69.   Cedervall, T., et al., *Detailed identification of plasma proteins adsorbed on copolymer nanoparticles.* Angew Chem Int Ed Engl, 2007. **46**(30): p. 5754-6.

70.   Moghimi, S.M., A.C. Hunter, and T.L. Andresen, *Factors controlling nanoparticle pharmacokinetics: an integrated analysis and perspective.* Annu Rev Pharmacol Toxicol, 2012. **52**: p. 481-503.

71.   Klein, J., *Probing the interactions of proteins and nanoparticles.* Proc Natl Acad Sci U S A, 2007. **104**(7): p. 2029-30.

72.   Aggarwal, P., et al., *Nanoparticle interaction with plasma proteins as it relates to particle biodistribution, biocompatibility and therapeutic efficacy.* Adv Drug Deliv Rev, 2009. **61**(6): p. 428-37.

73.   Norman, M.E., P. Williams, and L. Illum, *Influence of block copolymers on the adsorption of plasma proteins to microspheres.* Biomaterials, 1993. **14**(3): p. 193-202.

74.   Kim, H.R., et al., *Analysis of plasma protein adsorption onto PEGylated nanoparticles by complementary methods: 2-DE, CE and Protein Lab-on-chip system.* Electrophoresis, 2007. **28**(13): p. 2252-61.

75.   Ogawara, K., et al., *Pre-coating with serum albumin reduces receptor-mediated hepatic disposition of polystyrene nanosphere: implications for rational design of nanoparticles.* J Control Release, 2004. **100**(3): p. 451-5.

76.   Moghimi, S.M. and A.C. Hunter, *Recognition by macrophages and liver cells of opsonized phospholipid vesicles and phospholipid headgroups.* Pharm Res, 2001. **18**(1): p. 1-8.

77.   Taylor, P.R., et al., *Macrophage receptors and immune recognition.* Annu Rev Immunol, 2005. **23**: p. 901-44.

78.   Olivier, J.C., *Drug transport to brain with targeted nanoparticles.* NeuroRx, 2005. **2**(1): p. 108-19.

79.   Klibanov, A.L., et al., *Amphipathic polyethyleneglycols effectively prolong the circulation time of liposomes.* FEBS Lett, 1990. **268**(1): p. 235-7.

80.   Blume, G. and G. Cevc, *Liposomes for the sustained drug release in vivo.* Biochim Biophys Acta, 1990. **1029**(1): p. 91-7.

81.   Papahadjopoulos, D., et al., *Sterically stabilized liposomes: improvements in pharmacokinetics and antitumor therapeutic efficacy.* Proc Natl Acad Sci U S A, 1991. **88**(24): p. 11460-4.

82.   Michel, R., et al., *Influence of PEG architecture on protein adsorption and conformation.* Langmuir, 2005. **21**(26): p. 12327-32.

83.   Fang, F., J. Satulovsky, and I. Szleifer, *Kinetics of protein adsorption and desorption on surfaces with grafted polymers.* Biophys J, 2005. **89**(3): p. 1516-33.

84.   Cullis, P.R., A. Chonn, and S.C. Semple, *Interactions of liposomes and lipid-based carrier systems with blood proteins: Relation to clearance behaviour in vivo.* Adv Drug Deliv Rev, 1998. **32**(1-2): p. 3-17.

85.   Poon, Z., et al., *Layer-by-layer nanoparticles with a pH-sheddable layer for in vivo targeting of tumor hypoxia.* ACS Nano, 2011. **5**(6): p. 4284-92.

86.   Lee, E.S., Z. Gao, and Y.H. Bae, *Recent progress in tumor pH targeting nanotechnology.* J Control Release, 2008. **132**(3): p. 164-70.

87.   Sarkar, N., et al., *Matrix metalloproteinase-assisted triggered release of liposomal contents.* Bioconjug Chem, 2008. **19**(1): p. 57-64.

88.   Wong, C., et al., *Multistage nanoparticle delivery system for deep penetration into tumor tissue.* Proc Natl Acad Sci U S A, 2011. **108**(6): p. 2426-31.

89.   Wu, G., et al., *Remotely triggered liposome release by near-infrared light absorption via hollow gold nanoshells.* J Am Chem Soc, 2008. **130**(26): p. 8175-7.

90.   Paasonen, L., et al., *Gold nanoparticles enable selective light-induced contents release from liposomes.* J Control Release, 2007. **122**(1): p. 86-93.

91.   von Maltzahn, G., et al., *Nanoparticles that communicate in vivo to amplify tumour targeting.* Nat Mater, 2011. **10**(7): p. 545-52.

92.   Juliano, R., *Challenges to macromolecular drug delivery.* Biochem Soc Trans, 2007. **35**(Pt 1): p. 41-3.

93.   Agrawal, S., J. Temsamani, and J.Y. Tang, *Pharmacokinetics, biodistribution, and stability of oligodeoxynucleotide phosphorothioates in mice.* Proc Natl Acad Sci U S A, 1991. **88**(17): p. 7595-9.

94.   Nakada, Y., et al., *Pharmacokinetics and biodistribution of oligonucleotide adsorbed onto poly(isobutylcyanoacrylate) nanoparticles after intravenous administration in mice.* Pharm Res, 1996. **13**(1): p. 38-43.

95.   Beverly, M.B., *Applications of mass spectrometry to the study of siRNA.* Mass Spectrom Rev. **30**(6): p. 979-98.

96.   Chen, G., et al., *Characterization of protein therapeutics by mass spectrometry: recent developments and future directions.* Drug Discov Today, 2011. **16**(1-2): p. 58-64.

97.   Frangioni, J.V., *In vivo near-infrared fluorescence imaging.* Curr Opin Chem Biol, 2003. **7**(5): p. 626-34.

98.   Hilderbrand, S.A. and R. Weissleder, *Near-infrared fluorescence: application to in vivo molecular imaging.* Curr Opin Chem Biol. **14**(1): p. 71-9.

99.   Li, J., Y. Yang, and L. Huang, *Calcium phosphate nanoparticles with an asymmetric lipid bilayer coating for siRNA delivery to the tumor.* J Control Release.

100.   Mackiewicz, N., et al., *Tumor-targeted polydiacetylene micelles for in vivo imaging and drug delivery.* Small, 2011. **7**(19): p. 2786-92.

101.   Abdelmawla, S., et al., *Pharmacological characterization of chemically synthesized monomeric phi29 pRNA nanoparticles for systemic delivery.* Mol Ther, 2011. **19**(7): p. 1312-22.

102.   Goldberg, M.S., et al., *Nanoparticle-mediated delivery of siRNA targeting Parp1 extends survival of mice bearing tumors derived from Brca1-deficient ovarian cancer cells.* Proc Natl Acad Sci U S A, 2011. **108**(2): p. 745-50.

103.   Yang, Y., et al., *Systemic delivery of siRNA via LCP nanoparticle efficiently inhibits lung metastasis.* Mol Ther, 2012. **20**(3): p. 609-15.

104.   Graham, M.J., et al., *Tritium labeling of antisense oligonucleotides by exchange with tritiated water.* Nucleic Acids Res, 1993. **21**(16): p. 3737-43.

105.   Ballou, B., L.A. Ernst, and A.S. Waggoner, *Fluorescence imaging of tumors in vivo.* Curr Med Chem, 2005. **12**(7): p. 795-805.

106.   Zhao, J.K., Gao, C. Y., Liu, D. , *The extended Q-range small-angle neutron scattering diffractometer at the SNS.* Journal of Applied Crystallography, 2010. **43**: p. 1068-1077.

107.   Kline, S.R., *Reduction and analysis of SANS and USANS data using IGOR Pro.* Journal of Applied Crystallography 2006. **39**: p. 895-900.

108.   Damodaran, V.B., et al., *Conformational studies of covalently grafted poly(ethylene glycol) on modified solid matrices using X-ray photoelectron spectroscopy.* Langmuir, 2010. **26**(10): p. 7299-306.

109.   Gao, X., et al., *Chain conformation of a new class of PEG-based thermoresponsive polymer brushes grafted on silicon as determined by neutron reflectometry.* Langmuir, 2009. **25**(17): p. 10271-8.

110. Devanand, K. and J.C. Selser, *Asymptotic behavior and long-range interactions in aqueous solutions of poly(ethylene oxide).* Macromolecules, 1991. **24**(22): p. 5943-5947.

111. Woodle, M.C. and D.D. Lasic, *Sterically stabilized liposomes.* Biochim Biophys Acta, 1992. **1113**(2): p. 171-99.

112. Swain, P.S. and D. Andelman, *Supported membranes on chemically structured and rough surfaces.* Phys Rev E Stat Nonlin Soft Matter Phys, 2001. **63**(5 Pt 1): p. 051911.

113. Lipowsky, R., *The conformation of membranes.* Nature, 1991. **349**(6309): p. 475-81.

114. Allen, C., et al., *Controlling the physical behavior and biological performance of liposome formulations through use of surface grafted poly(ethylene glycol).* Biosci Rep, 2002. **22**(2): p. 225-50.

115. Cabral, H., et al., *Accumulation of sub-100 nm polymeric micelles in poorly permeable tumours depends on size.* Nat Nanotechnol, 2011. **6**(12): p. 815-23.

116. Monopoli, M.P., et al., *Physical-chemical aspects of protein corona: relevance to in vitro and in vivo biological impacts of nanoparticles.* J Am Chem Soc, 2011. **133**(8): p. 2525-34.

117. Gref, R., et al., *'Stealth' corona-core nanoparticles surface modified by polyethylene glycol (PEG): influences of the corona (PEG chain length and surface density) and of the core composition on phagocytic uptake and plasma protein adsorption.* Colloids Surf B Biointerfaces, 2000. **18**(3-4): p. 301-313.

118. Senior, J.H., *Fate and behavior of liposomes in vivo: a review of controlling factors.* Crit Rev Ther Drug Carrier Syst, 1987. **3**(2): p. 123-93.

119. Akinc, A., et al., *Targeted delivery of RNAi therapeutics with endogenous and exogenous ligand-based mechanisms.* Mol Ther, 2010. **18**(7): p. 1357-64.

120. Baratta, J.L., et al., *Cellular organization of normal mouse liver: a histological, quantitative immunocytochemical, and fine structural analysis.* Histochem Cell Biol, 2009. **131**(6): p. 713-26.

121. Snoeys, J., et al., *Species differences in transgene DNA uptake in hepatocytes after adenoviral transfer correlate with the size of endothelial fenestrae.* Gene Ther, 2007. **14**(7): p. 604-12.

122. Hak, S., et al., *The effect of nanoparticle polyethylene glycol surface density on ligand-directed tumor targeting studied in vivo by dual modality imaging.* ACS Nano, 2012. **6**(6): p. 5648-58.